universität wien

MASTERARBEIT / MASTER'S THESIS

Titel der Masterarbeit / Title of the Master's Thesis

„Design and Preparation of Noise Measurements in the Anomalous Metal Phase"

verfasst von / submitted by

Kristen Williams Galvin

angestrebter akademischer Grad / in partial fulfilment of the requirements for the degree of

Master of Science (MSc)

Wien, 2023 / Vienna, 2023

Studienkennzahl lt. Studienblatt / degree programme code as it appears on the student record sheet:	UA 066 876
Studienrichtung lt. Studienblatt / degree programme as it appears on the student record sheet:	Masterstudium Physik
Betreut von / Supervisor:	Univ.-Prof. Dr. Norbert Schuch

Acknowledgements

First and foremost I would like to thank Prof. Andrew Higginbotham of the Institute of Science and Technology Austria for his support and supervision of this thesis, including the use of his labs and office space. This thesis would not be possible without his ideas and endless energy. Thank you for showing me the way towards becoming a good scientist, and having patience while teaching me even very basic details. I also offer many thanks to PhD student Duc Phan who fabricated the samples used in this project. Many thanks also to all members of the Higginbotham group who have helped in small ways and provided camaraderie along the way. I look forward to continuing to work with you all in the future!

Many thanks also to Prof. Norbert Schuch for agreeing to be my official supervisor at the University of Vienna. Your help in navigating the master thesis process has been key to completing this thesis. I thank also my friends in Vienna who have made the move to Austria as smooth as it could be, and for the fun times we have shared together. I also could not have gotten to where I am now if not for my family, who I thank for always supporting me even from a continent and six time zones apart. Last of all I thank you, Julian, for always being by my side.

Abstract

Anomalous metals are materials that exhibit unusual transport behavior at low temperatures that cannot be explained by Fermi liquid theory. They occur in thin-film superconductors that have been tuned non-thermally out of the superconducting state. While they have been subject of active research in condensed matter physics over the past three decades, there are still many questions that remain open. One promising approach to improve our understanding of their effective charge carriers is to carry out charge noise measurements on these samples.

This thesis reports on the design and realization of a new device to perform such noise measurements. Through several iterations, we developed a printed circuit board (PCB) for the efficient readout of microwave signals. The design was guided by the requirements of minimizing insertion loss and resonances over the required frequency range. We present detailed measurements on the PCBs' transmission spectra at each iteration. The PCB was then used in conjunction with a new low-frequency microwave readout chain to test the proper functioning of the anomalous metal device, whose suitable performance was verified with IV characteristics and measurements of the gate-dependent resistance. In future experiments, the device reported on here will be used for measurements concerning the noise of the anomalous metal phase.

Kurzfassung

Anomale Metalle sind Materialien, die bei niedrigen Temperaturen ein ungewöhnliches Transportverhalten zeigen, das sich nicht mit der Fermi-Flüssigkeits-Theorie erklären lässt. Sie treten in Dünnschicht-Supraleitern auf, die nicht-thermisch aus dem supraleitenden Zustand herausgefahren wurden. Obwohl sie in den letzten drei Jahrzehnten im Zentrum der Forschung zur Physik der kondensierten Materie standen, sind noch viele Fragen offen. Ein vielversprechender Ansatz zur Verbesserung unseres Verständnisses ihrer effektiven Ladungsträger ist es Messungen des Ladungsrauschens in diesen Proben durchzuführen.

Diese Arbeit berichtet über den Entwurf und die Realisierung eines neuen Chips zur Durchführung solcher Rauschmessungen. In mehreren Iterationen haben wir eine Leiterplatte für das effiziente Auslesen von Mikrowellensignalen entwickelt. Ziel des Designs ist es, Eingangsverlust und Resonanzen über den erforderlichen Frequenzbereich zu minimieren. Wir präsentieren detaillierte Messungen der Transmissionsspektren der Leiterplatten jeder Iteration. Die Leiterplatte wurde dann in Verbindung mit dem anomalen Metall-Chip verwendet, dessen ordnungsgemäße Funktion anhand von Strom-Spannungs-Kennlinien und Messungen des Widerstands in Abhängigkeit von der Gate-Spannung überprüft wurde. In zukünftigen Experimenten wird dieser Chip für Messungen des Rauschens der anomalen Metallphase verwendet werden.

Contents

1. Introduction

Considering the abundance of activity in superconductivity research, it is remarkable how little is actually known about the nature of superconductors. We think we understand how conventional type I three-dimensional superconductors behave, and why. But every decade since the first discovery of superconductors has brought more discoveries and more inexplicable behavior. The interest in researching superconductors has only increased in the decades since their discovery, and for good reason. Superconductivity has the potential to revolutionize daily life, in applications as far reaching as magnetically levitated ultrafast trains to medical imaging and quantum computing to incredibly efficient energy systems. Some of these applications are already realized, and many more are predicted to arise as our understanding of superconductors deepens.

Despite great progress being made in many branches of superconductivity research, the question of the anomalous metal remains open. First observed in the 1980s, physicists still debate the origins and causes of this phase. What could be causing a superconductor to unexpectedly begin behaving like a metal? And what's more, behaving like a metal in a regime where metals are supposedly forbidden to exist? After thirty years and many experiments observing the same phenomenon across countless varied platforms, we are still searching for answers to basic questions about this phase of matter. One such basic question concerns noise signatures. While the behavior of noise in the superconducting state is well understood, noise in the anomalous metal phase has yet to be probed. This thesis seeks to prepare to answer the question: what form does noise take in the anomalous metal phase? Experimental results to this effect have not yet been published, and the answer may unlock keys to understanding the nature of this phase.

The format of this thesis is as follows: First there will be a brief theoretical introduction to the topic of superconductivity, especially two-dimensional superconductors, and what is currently known about the anomalous metal phase. Background information on the topics of Josephson junctions will also be covered. In the second chapter the basics of the experimental methods will be introduced, including how dilution refrigerators work and how the samples used in this project are made using nanofabrication. In the third chapter, the experimentation of printed circuit boards including tests of a novel on-board bias tee for simultaneous gigahertz and DC probing of samples will be presented. Chapter four covers the installation of a new microwave readout chain in a dilution refrigerator, and chapter five presents the results of both a calibration device and the real experimental device. Lastly, the conclusions of the project and outlook for this line of research will be discussed.

1.1. Conventional Superconductivity

The study of superconductors began with Heike Kamerlingh Onnes' 1911 discovery that the resistance of a solid block of mercury suddenly reduced to zero below a 'critical' temperature of 4.2 K. Over the following decades more superconducting elements were discovered, all with differing critical temperatures. In 1933 Fritz W. Meissner and Robert Ochsenfeld discovered the second signature of superconductivity - that superconductors expel all magnetic fields from their interiors and cannot be penetrated by applied magnetic fields. At this point more than two decades had passed since Onnes' discovery, and a theoretical framework to understand the behavior was still lacking. Finally in 1935 the brothers Fritz and Heinz London managed to explain Meissner and Ochsenfeld's results with two classical equations, known as the London equations. They sought a replacement for Ohm's law that would apply to superconductors and came up with curl $\lambda \mathbf{j} = -\frac{1}{c}\mathbf{H}$, for $\lambda = -n_s \frac{e^2}{m_e}$ where $\mathbf{j}$ is the current, c is the speed of light, $\mathbf{H}$ is the magnetic field strength, n_s is the density of superconducting electrons, m_e is the electron mass, and e is the electron charge[1]. This equation was later formulated as curl $\mathbf{j} = -\frac{1}{\mu_0 \lambda_L^2}\mathbf{B}$ in SI units, where $\lambda_L \neq \lambda$, and the meaning of λ_L will be explained later[2]. This is the first London equation, which mathematically explains the Meissner effect (the expulsion of magnetic fields from a superconductors' bulk). Following the derivation in [2], we consider the Maxwell equation:

$$\mu_0 \mathbf{j} = \text{curl } \mathbf{B} \tag{1.1}$$

Take the curl of both sides and combine with the first London equation, then simplify:

$$\text{curl } \mathbf{j} = \frac{1}{\mu_0} \text{ curl curl } \mathbf{B} = -\frac{1}{\mu_0 \lambda_L^2}\mathbf{B} \tag{1.2}$$

$$\nabla^2 \mathbf{B} = \frac{\mathbf{B}}{\lambda_L^2} \tag{1.3}$$

The final equation restricts constant solutions $\mathbf{B}(r) = B_0$ to the case $B_0 = 0$, because while $\frac{B_0}{\lambda_L^2}$ can take any value, $\nabla^2 \mathbf{B}$ can only be zero. This implies that a uniform magnetic field cannot exist inside of a superconductor. In fact the London brothers also proved that superconductors are perfect diamagnets, meaning that they will generate a screening current to exactly cancel any applied magnetic field. The derivation of the second London equation is much longer, but it is written as $\frac{d\mathbf{j}}{dt} = \lambda \mathbf{E}$ and shows that the rate of change of the current in a superconductor is proportional to the electric field.

However, magnetic fields can permeate some distance into a superconductor from the surface. A magnetic field penetrates exponentially to a depth given by λ_L, a quantity derivable from the above London equation. A solution to $\nabla^2 \mathbf{B} = \frac{\mathbf{B}}{\lambda_L^2}$ for a parallel magnetic field reads

$$\mathbf{B}(r) = B_0 e^{-\frac{r}{\lambda_L}} \tag{1.4}$$

assuming a near-infinite superconductor and that the field has a strength of B_0 at the

boundary of the superconductor. It can be derived as in [2] that

$$\lambda_{\mathrm{L}} = \sqrt{\frac{\epsilon_0 m_{\mathrm{e}} c^2}{n_{\mathrm{s}} q^2}} \tag{1.5}$$

in SI units. The London penetration depth depends on the number of superconducting electrons, so as a superconductor is heated closer to the critical temperature, the penetration depth will increase. When the number of superconducting electrons reaches zero, magnetic fields can penetrate the entire depth of the superconductor. The calculated λ_{L} values for some common superconductors are between 10 and 100 nm[2].

This great success in mathematically explaining the expulsion of magnetic fields from inside superconductors was followed by another twenty years of little theoretical progress. It wasn't until the 1950s that a quantum theory of conventional superconductivity was developed. In 1950 Lev Landau and Vitaly Ginzburg proposed that a Schrödinger-like function could govern a superconductor's order parameter, and derived a theory to understand superconductor's behavior without considering microscopic properties. The order parameter contains information on the intrinsic properties of the superconductor, and the Ginzburg-Landau (GL) equation describes the spatial properties of the superconductor[3]. The GL equation led to the formulation of the coherence length of a superconductor, and the application of wave functions to the context of superconductors. The theory works for temperatures close to the critical temperature, and over a spatial extent where the order parameter does not vary too much[4]. The coherence length of a superconductor is a characteristic length scale of a superconductor, separate from the penetration depth. It measures the distance over which a material transitions from normal to superconductor, the spatial extent to which the density of superconducting electrons are affected by applied magnetic fields. Pure superconductors have a coherence length equal to the *intrinsic coherence length*:

$$\xi_0 = \frac{2\hbar v_{\mathrm{F}}}{\pi E_{\mathrm{g}}} \tag{1.6}$$

where v_{F} is the Fermi velocity and E_{g} is the superconducting energy gap. In impure materials or alloys, the coherence length is shorter than ξ_0 and is a function of temperature given by

$$\xi(T) = \sqrt{\frac{\hbar^2}{2m_* a(T)}} \tag{1.7}$$

where $a(T)$ is a constant of the form $a_0(T - T_{\mathrm{c}})$ derived from the GL equation, and m_* is the effective mass of the charge carriers. Some common superconductors' coherence lengths measure between 40-160 nm[2]. Together the penetration depth and the coherence length give a clear idea of the length scales relevant to the superconductor-normal transition and are important characteristics of superconductors. It is easy to imagine that as the thickness of a superconductor approaches either of these length scales, interesting behavior could result that differs from typical superconductor behavior.

Ginzburg-Landau theory covers the quantum mechanical understanding of superconductivity, but what about an intuitive understanding of transport in superconductors? In 1957 John Bardeen, Leon Cooper, and John Schrieffer came up with a microscopic theory of superconductivity, a breakthrough in the physical understanding of superconductors. The year before, in 1956, Cooper demonstrated that the Fermi sea of electrons has a propensity towards forming bound pairs, if there is an attractive interaction[5]. The binding energy of a Cooper pair of electrons can be derived to find

$$\Delta = \frac{2\hbar\omega_{\mathrm{D}}}{\exp(1/N_{\mathrm{F}}V) - 1} \tag{1.8}$$

where ω_{D} is the Debye phonon cutoff frequency, N_{F} is the density of states at the Fermi energy, and V is the potential. If V is positive, it is an attractive potential and energy in the system will be minimized by pairing of electrons above the Fermi level. The Fermi gas of electrons in a superconductor is therefore unstable, and will continuously allow the pairing of electrons[2]. This binding energy is closely related to the superconducting energy gap[4].

This set the stage for the development of the full BCS (named for Bardeen, Cooper, and Schrieffer) theory. In the superconducting state, BCS theory prescribes that as an electron travels through the material it deforms the lattice around it, which can be represented as a phonon. This creates an attractive potential, pulling another electron toward it, forming a correlated electron pair despite the normal repulsion between electrons. These Cooper pairs can be thought of as travelling through the material together. Then, the number of bound pairs of electrons increases until a condensate is formed. This condensate is robust against pair breaking, because the energy required to break a single pair becomes the energy required to break all pairs simultaneously. Due to this, the normal sources of resistance in a conductor are not energetic enough to cause resistance in a superconductor and electron pairs are able to conduct infinitely. In this way, BCS theory explains that superconductivity results from electron-phonon interaction[6],[7],[4]. Beyond the simple picture presented here, Cooper pairs are pairs of electrons of opposite spin and opposite momentum, and so do not literally travel through the material alongside one another. They can often be treated as bosons, as together they have a total spin of zero.

The transition from normal to superconductor at zero applied magnetic field is a second order phase transition, as the superconducting energy gap (which arises from the electron-electron interaction) reduces continuously as the density of superconducting electrons reduces[2]. However, a superconductor can also transition to a normal state by application of a strong enough magnetic field or current. When a large enough field is applied, the generated screening current will be energetic enough to destroy the superconductivity. Upon reaching a field strong enough to generate an energy comparable to the superconducting energy gap, the electron of spin opposite to the direction of the field will be unable to resist aligning itself with the field. This leads to the destruction of the bond between the two electrons, and a breakdown of superconductivity[4]. The field at which superconductivity is broken is called

the critical field, and is temperature dependent. There are some materials that undergo an intermediary transition upon application of a magnetic field, in which some magnetic field is allowed to penetrate the bulk of the superconductor in the form of vortices. Vortices are quantized flux trapped in a superconducting bulk. As the applied magnetic field climbs even higher, more vortices enter the superconductor until the superconductivity is eventually broken. The field at which the vortices begin to enter the superconductor is the lower critical field, while the field at which superconductivity is entirely destroyed is the upper critical field. In general, superconductors that experience only one critical field are classified as type I superconductors, while those that experience an intermediate phase between two critical fields are type II superconductors. Type I superconductors have a penetration depth less than the coherence length and type II superconductors have a coherence length less than the penetration depth. Type II superconductors' critical fields can be related to one another by

$$H_{c1} \approx \frac{\xi}{\lambda} H_c \tag{1.9}$$

$$H_{c2} \approx \frac{\lambda}{\xi} H_c \tag{1.10}$$

where $H_{c1} < H_c < H_{c2}$[2]. Where H_c is the extrapolated critical field of the material, if vortices were not able to enter (see the sketch in figure 1.1). Typically type II superconductors have a higher critical temperature, and are suitable for use in many applications such as superconducting magnets.

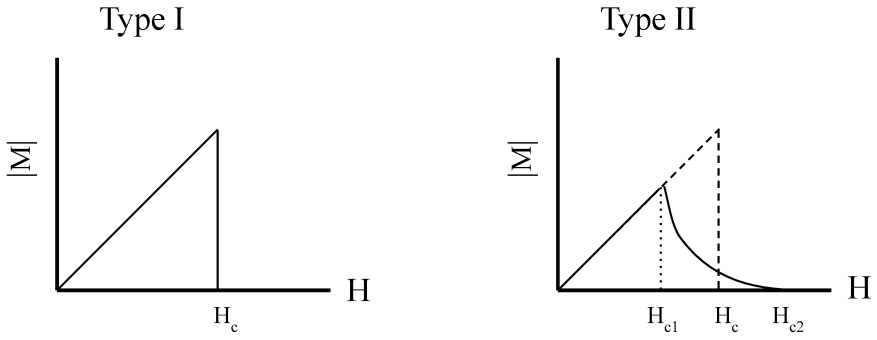

Figure 1.1.: Types of superconductors. Type I superconductors become negatively magnetized linearly with applied magnetic field. Type II superconductors experience the invasion of vortices. Between the zero and the lower critical field there is a global superconducting state. Between the two critical fields is a vortex state, and above the upper critical field is a normal state.

To this day BCS theory is considered a triumph, it manages to explain the mechanism of conventional superconductivity microscopically. And combined with the Ginzburg-Landau equation, conventional superconductors are reasonably well-understood on both classical and quantum levels. However, both theories suffer from some degree of simplification, and apply mainly to low temperature s-wave superconductors. Several decades after GL theory and BCS theory were developed, high-temperature superconductors were discovered and the usual

theories could no longer explain their behavior. This lead to the classification of conventional and unconventional superconductors and has pre-occupied condensed matter physics ever since.

1.2. Unconventional Superconductivity

The usual mechanisms for understanding superconductivity proved insufficient when in the 1980s so-called high temperature superconductors were discovered, with critical temperatures reaching even above 100 K, far above the previous record-highs in the low 20s of kelvins[8],[9],[10]. These newly discovered superconductors are today called cuprate superconductors, because they occur in a family of copper oxide/metal oxide layered materials. They achieve the highest critical temperatures of all known superconductors at normal pressures, but the explanation continues to puzzle condensed matter physicists to this day, and is an area of highly active research. Since the 1990s other kinds of unconventional superconductors have also been established, such as holographic superconductivity[11], ceramic superconductors[12], iron-based superconductors[13], and even superconductivity resulting from twisting the layers of bilayer graphene to the 'magic' angle of 1.1 degrees relative to one another[14].

Superconductors also begin to behave differently when their thickness is reduced to the order of their coherence length or penetration depth. These so-called "thin-film superconductors" can even be thinner than their penetration depth, allowing magnetic fields to penetrate uniformly through the entire superconductor. The behavior in this case deserves careful consideration. In the 1980s, experiments were performed on thin-film superconductors, such as the work by Heinrich M. Jaeger on ultrathin granular metal films of thicknesses in the tens of angstroms[15]. He and his colleagues discovered that instead of transitioning abruptly from insulating to superconducting behavior as they increased the thickness of their films, there appeared some intermediary "metallic" phase. Metallic in the sense that the resistance of the samples saturated to some finite value, instead of dropping to zero or increasing to some "infinite" value indicating insulating behavior. This was wholly unexpected, and has been seen time and time again in the decades since. The coming sections will explore the superconductor to insulator transition and the anomalous metal phase in more detail.

1.2.1. Superconductor-Insulator Transition

In general, when the conditions for superconductivity are no longer met, a superconductor will cease to repel external magnetic fields, and cease to exhibit zero resistivity. Many common metals such as tin, lead, mercury, and aluminum are superconductors in two-dimensions at low temperatures, but when the superconductivity is broken due to e.g. a large applied magnetic field overcoming the binding energy of the Cooper pairs, they will become insulators because there is still a gap in the density of states. The superconductor to insulator transition is an example of a quantum phase transition.

The superconductor to insulator quantum phase transition is driven by a significant change

occurring in the behavior of the electrons upon tuning a parameter of the Hamiltonian at zero temperature. It is a quantum phase transition, because it is driven not by thermal fluctuations but by quantum fluctuations[16]. This is in contrast to the continuous (classical) phase transition experienced by superconductors as the temperature is increased above T_c. In a continuous phase transition, the superconducting order parameter undergoes a smooth transition from $\psi = \psi_{max}$ at zero temperature to $\psi = 0$ at the critical temperature, and is complete when the correlation length of the superconductor diverges at $T = T_c$ as

$$\xi \sim t^{-\nu} \tag{1.11}$$

where $t = |T - T_c|/T_c$ and ν is the correlation length critical exponent[16]. A phase transition's behavior at the critical point is determined entirely by its full set of critical exponents, which can be derived from the two independent exponents: correlation length ν and correlation function η. The critical exponents control the physics of the phase transition near criticality, and among them the correlation length critical exponent is the most important.

When considering whether a phase transition is quantum or not, it is important to note the energy scales involved. In general, if the energy of thermal fluctuations $k_B T$ is greater than the quantum energy scale $\hbar\omega$ (where ω is a characteristic frequency of the system), then the transition will be classically driven, and vice versa. The quantum energy scale $\hbar\omega$ varies with temperature as

$$\hbar\omega \propto |t|^{\nu z} \tag{1.12}$$

where z is the dynamical critical exponent. So for a distance away from the critical temperature defined by

$$t_x \propto T_c^{\frac{1}{\nu z}} \tag{1.13}$$

a crossover point from quantum to classical phase transition will be reached[16]. This is why transitions at zero (or very close to zero) temperature are dominated by quantum fluctuations and transitions above the crossover point t_x and near to the critical temperature depend entirely on classical fluctuations. In the case of the superconductor to insulator transition, a distance from the critical point cannot be defined in terms of temperature. Instead it is defined by whichever parameter is being tuned, such as pressure, film thickness, applied magnetic field, or gate voltage, in the form $t = |q - q_c|/q_c$ where q represents the tuning parameter and q_c is the critical value of that parameter.

Another important factor to consider when discussing phase transitions is the dimensionality of the system. Renormalization group theory (from which critical exponents and the theoretical understanding of phase transitions stem) shows that above some upper critical dimension, the fluctuations that drive a phase transition become irrelevant and the behavior of the phase transition equals that of mean-field theory. And below some lower critical dimension, there is no phase transition because the ordered phase is overcome by the fluctuations[17]. The interesting physics of phase transitions occurs entirely within the two critical dimensions.

As a consequence, a direct superconductor to insulator transition is observed only in two dimensions. The next section will discuss the anomalous metallic phase that arises in many cases of the two dimensional superconductor to insulator transition.

1.2.2. Two-Dimensional Superconductivity

While the physics of bulk superconductors in three dimensions is relatively well understood, when the thickness of a superconductor is reduced to essentially two dimensions (where the thickness reaches the order of the penetration depth) the behavior becomes less well defined. There has been an abundance of research on thin-film superconductors in the last thirty years. The variety of materials and sample platforms studied is vast. Many different experiments have been performed studying the superconductor to insulator transition in thin films, using a wide variety of tuning parameters. In part due to the many different 'knobs' available to experiment with in two-dimensions, coming up with some kind of unifying model for two-dimensional superconductors has so far been out of reach[18].

However, some characteristics are known, for example if a superconductor is thinner than its penetration depth, a uniform magnetic field is allowed to exist within the entirety of the superconductor. In such a case, the complete Meissner effect is not observed. Thin-films are still said to display global superconductivity at zero magnetic field because they do exhibit other properties of superconductors such as the continuous phase transition at T_c to a state with zero resistivity. In fact, due to the incomplete Meissner effect, thin films generate only a small screening current against any applied field. This small current isn't energetic enough to disturb the bound pairs of electrons, and therefore a much higher magnetic field will need to be applied in order to break the superconductivity of a thin film in comparison to a three-dimensional superconductor[2]. In short, thin films have higher critical fields than three-dimensional superconductors.

It is also thought that some two-dimensional superconductors undergo a Berezinskii-Kosterlitz-Thouless type transition at a temperature $T_{BKT} < T_c$. This is a phase transition in which vortex-antivortex pairs in the superconductor become unpaired after some critical temperature is reached. As the thermal energy of the superconductor increases, the vortex-antivortex pairs will begin to move away from one another until they separate entirely, which results in the development of a nonzero resistance[19]. This analogous to the breaking of Cooper pairs at sufficient energies in three-dimensional superconductors. The temperature can be calculated by

$$T_{BKT} \approx \frac{\Phi_0^2}{32\pi^2\lambda_\perp} \tag{1.14}$$

where Φ_0 is the flux quantum and $\lambda_\perp$ is the Pearl length[4]. Since the Pearl length is thickness-dependent, the BKT transition temperature also depends on the thickness of the

superconductor.

$$\lambda_{\perp} = \frac{2\lambda_{\mathrm{L}}^2}{d} \tag{1.15}$$

$$T_{\mathrm{BKT}} \propto \frac{d}{\lambda_{\mathrm{L}}^2} \tag{1.16}$$

T_{BKT} decreases proportionally to the thickness of the sample. This decrease of critical temperature with decreasing sample thickness was observed by Haviland, Liu, and Goldman in 1989[20]. The BKT transition is thought to be the origin of thin films having lower critical temperatures than three-dimensional superconductors.

Throughout the literature there does seem to develop two categories of two-dimensional superconductors: those which undergo a direct superconductor to insulator transition and those which undergo an intermediate phase transition, from superconductor to metal to insulator transition. The nature of the superconductor-metal-insulator transition is especially puzzling, as it is theorized that metals cannot exist in dimensions less than three. Yet this phase is seen in many different systems via many different tuning parameters. There must be some explanation for this apparent metallic state, but so far there is little agreement on proposed theories.

1.2.3. Anomalous Metals

In Fermi liquid theory, there are two types of excitations that contribute to conductivity: fermionic and bosonic excitations. But at very low temperatures only the fermionic excitations, or quasiparticles, make a contribution because the density of states of the bosonic excitation drops to zero[21]. In typical Fermi liquids at low temperatures, conductivity is dominated by Umklapp processes (electron scattering off phonons) and electron-electron scattering. This leads to a resistivity dependence of T^2, and a linear dependence of the specific heat with temperature[2].

The other successful theory of metals is the Drude model. The Drude model for metals relatively accurately specifies values of conductance for different metals using classical scattering theory. The Drude conductivity is given by the formula

$$\sigma_{\mathrm{D}} = e^2 D n \tag{1.17}$$

where n is the electron density of states at the Fermi energy, and D is the diffusion coefficient given by

$$D = \frac{v_{\mathrm{F}} l}{3} \tag{1.18}$$

[21]. The Drude model doesn't predict resistivity at low temperatures very well, because it is a kinetic theory that relies on scattering events which are temperature dependent but the theory itself doesn't account for temperature.

Neither the Drude model nor Fermi liquid theory are able to predict the values of resistance that are seen in the anomalous metal phase that is observed. And moreover, many physicists believe that the Hohenberg-Mermin-Wagner (HMW) theorem implies that true metals cannot exist in dimensions less than three. The theorem excludes the possibility of long-range order in lower dimensional materials due to a lack of spontaneous symmetry breaking in dimensions less than three. Since superconductivity is a symmetry-breaking state (breaking of the electromagnetic gauge invariance), the HMW theorem would disallow the existence of superconductors in two dimensions[22]. However, thanks to the work of Berezinskii, Kosterlitz, and Thouless, it has been shown that a BKT transition can occur in two-dimensional systems allowing superconductivity to occur without long-range order. According to the HMW theorem, in metals (which have long range order) the fluctuations that are entropically favored in dimensions less than three would destroy their order and exclude their existence[23],[24]. Additionally, based on arguments of the scaling theory of localization, the presence of even the smallest amount of disorder is enough to destroy the long-range order of metals in two dimensions[25],[26]. The depth of evidence surrounding the apparent metallic phase in two-dimensional superconductors thence either suggests a new phase of matter separate from that of Fermi liquids, or requires a re-working of current theories of metals[21],[27].

One early observation of the anomalous metal phase was in 1989 by H.M. Jaeger in a series of thin film experiments observing the superconductor to insulator transition[15]. They observed insulating thin films whose resistance went toward infinity as temperature went to zero ($\sim$0.6 K). As they deposited more layers onto the thin films, they noticed that the resistance of the samples saturated to a finite value, even as the temperature decreased to zero. Then, as the samples became thick enough, they observed typical superconducting behavior where the resistance dropped to zero at the critical temperature. This entire transition occurred over a few angstroms in thickness. This was a surprise, as while the samples were getting thicker, they were still in the realm of thin-films and two-dimensional materials where a metallic phase is forbidden. As scientists investigated further, they found evidence for this phase in all kinds of different experiments. Its signatures are not restricted to experiments of film thickness but have also been observed under tuning of the magnetic field in amorphous MoGe films of 30Å[28], tuning of carrier density via gate voltage in two-dimensional electron gases[29] and in monolayer flakes of WTe_2[30], among other systems.

The key distinguishing signature of this phase is a drop in the resistance as the temperature is cooled below the critical temperature of the superconductor followed by a saturation of the zero-temperature resistance to a value controllable with a tuning parameter. This response is nearly always seen as an intermediate phase, on the way from superconducting to insulating. This resistance saturation defies the otherwise successful Fermi liquid theory and Drude model, who set other predictions for conductivity of three-dimensional metals, and what value the resistances should take.

Beyond the observation of finite resistance, other signatures of the anomalous metal phase have

been investigated. These include the observation of a giant positive magnetoresistance[31], an anomalous Hall response (vanishing Hall resistivity)[32], and anomalous finite frequency conductivity (results consistent with transition to a metallic state[33], and non-Drude electrodynamics[34]). It is also predicted that the noise of the anomalous metal phase will reveal its own signature form, which would have decisive impacts on its interpretation[35]. There is additionally at least one proposal of using the anomalous metal quantum critical system to study non-equilibrium current noise as a dual to Hawking radiation[36]. There is clearly much work still to be done in investigating the anomalous metal phase, and many interesting implications of further study.

The final section of the introduction will discuss Josephson junction arrays, as this is the platform used in this thesis project.

1.3. Josephson Junction Arrays

In the 1960s Brian D. Josephson predicted that a superconducting current could tunnel through an insulating barrier, called a weak link. He came up with two important equations to describe this behavior, the DC Josephson effect and the AC Josephson effect. His prediction was proven correct and since then 'Josephson junctions' have been used in numerous applications including sensitive magnetic field detection (SQUIDs)[37], single-electron transistors[38], and superconducting qubits[39]. Experimentation with Josephson junctions has been active since the 1960s, and continues to this day. The platform used in this thesis project involves Josephson junction arrays, in which Josephson junctions are arranged in a two-dimensional array. The advantage of using a Josephson junction array is that they behave as ideal two-dimensional superconductors in which the phase-ordering (BKT) transition can be observed[40]. In typical thin films the phase-ordering transition is not observable due to fluctuations on the size of the order parameter and large amounts of disorder. This section will explain the DC and AC Josephson effects, and the physics of Josephson junction arrays.

In order to continue the discussion of the Josephson effect in superconductors, the concept of a superconducting phase must be introduced. Ginzburg-Landau theory treats a superconducting system with a Schrödinger-like equation. The 'wave-function', or the superconducting order parameter ψ can be thought of as a complex wavefunction,

$$\psi(r) = \psi_0 e^{i\phi(r)} \tag{1.19}$$

with amplitude ψ_0 and superconducting phase ϕ, and describes the behavior of all electrons in the system. The order parameter $\psi = \psi_{\max}$ when in the superconducting state and $\psi = 0$ in the normal state. The density of superconducting electrons locally is represented by $|\psi(r)|^2$. Importantly, the phase is a global phase of the entire superconductor and as such has no *intrinsic* meaning. A superconductor's phase only matters when spoken of in terms of a phase difference. This will become important in the Josephson effect.

The DC Josephson effect states that a zero-voltage supercurrent I_s is related to the phase difference across a weak link by

$$I_s = I_c \sin \Delta\phi \tag{1.20}$$

The critical current I_c is the maximum supercurrent that can pass through the junction. The critical current is determined by the material used, and the nature of the weak link (size, transport properties). But the critical current is bounded from below by the thermal energy, such that $I_c > 2ek_BT/\hbar$. Otherwise, thermal fluctuations due to the phase difference will dominate the phase-dependence of the current.[4]. In general, the critical current is also dependent on temperature, and is only at zero temperature the ideal junction critical current[40]. This equation can be derived from the time-dependent Schrödinger equation applied to the superconducting order parameters on either side of the weak link. Then, $\Delta\phi$ is the difference between the phases of the superconductors on either side of the weak link. This means that at zero applied voltage, a current will flow from one superconducting electrode to the next, and it will take a value between $-I_c$ and I_c depending on the phase difference between electrodes[2].

In contrast, the AC Josephson effect applies at non-zero voltages. Josephson predicted that if a voltage difference is applied across the junction, the phase difference of the junction would develop as

$$\frac{d\Delta\phi}{dt} = -\frac{2eV}{\hbar} = -\frac{2\pi}{\Phi_0}V \tag{1.21}$$

where $\Delta\phi = \phi_2 - \phi_1$, and $\Phi_0 = h/2e$ is the flux quantum. This can be derived from again applying the time-dependent Schrödinger equation to a superconductor whose electrons face a potential energy difference. The integration of both sides of the above equation yields a result for the phase difference of the junction under a non-zero voltage

$$\phi(t) = \phi(0) - \frac{2eVt}{\hbar} \tag{1.22}$$

Applying this to the first Josephson equation we arrive at the AC Josephson effect,

$$I_s = I_c \sin\left[\phi(0) - \frac{2eVt}{\hbar}\right] \tag{1.23}$$

where the current modulates as $\omega = 2eV/\hbar$[2]. This effect implies that the energy cost of a Cooper pair travelling across the junction is $h\omega$[4]. In figure 1.2, the current-voltage relation for a Josephson junction is shown. The DC Josephson effect can be seen as at zero voltage, the supercurrent can increase until a critical current I_c is reached, at which point no further current can be added. Then, after a certain voltage V_c (related to the BKT transition temperature) the AC Josephson effect kicks in and the junction becomes resistive. The current then oscillates with frequency $\omega = 2eV/\hbar$[2]. Lastly, the energy stored in the junction is given by

$$E(\phi) = -\frac{\Phi_0 I_c}{2\pi}\cos\phi \tag{1.24}$$

where the coupling, or Josephson, energy is given by $E_J = \Phi_0 I_c/2\pi = \hbar I_c/2e$[4]. The coupling energy can be thought of as the work needed to change the phase difference of the junction by $\pi/2$. It should also be noted that at all non-zero temperatures the junction will be slightly resistive due to the interaction of quasiparticles[40]

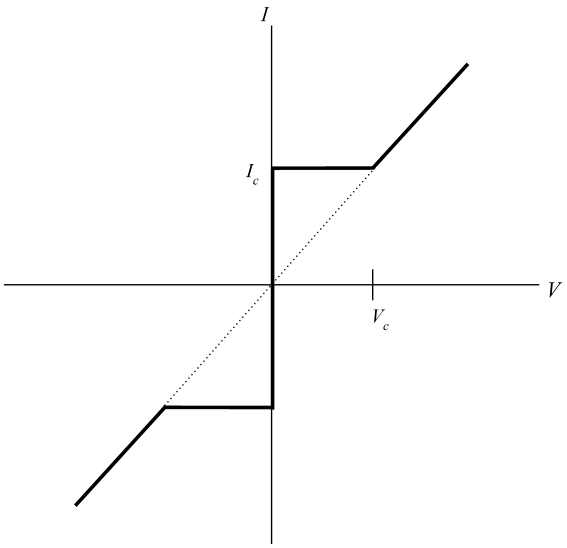

Figure 1.2.: Current-voltage curve for a Josephson junction.

Josephson junctions were first predicted to be formed with an insulator as the weak link, but they can also be formed using a normal (non superconducting) metal, or by forming a Dayem bridge[41], which is simply done by lessening the thickness of the superconducting material between two larger sections. This is possible due to tunneling of the Cooper pairs through the junction. They are used as single junctions, in chains of many junctions one after another, and in two-dimensional arrays of junctions. In many cases they are modeled by the resistively-and-capacitively-shunted junction model (RCSJ Model), as shown in figure 1.3. In this model the shunt capacitor reflects the geometric capacitance between the two superconducting islands, and the voltage-dependent shunt resistance is the effective resistance of the junction[4]. The charging energy of the capacitor in this model is given by $E_C = e^2/2C$, and can be ignored so long as the coupling energy E_J is much greater than the charging energy[40].

An array of Josephson junctions is an interesting two-dimensional superconductor. With it, one can study the frustrated XY model, different phase transitions, and vortex dynamics, among other important physics[40]. Aside from the edges, every superconducting island has four nearest neighbors that are connected via weak links, each with coupling energy E_J, see figure 1.4. The unit cell comprising four junctions of such an array forms what is known as a plaquette. Then summing over the phase differences across each junction in the plaquette gives $2\pi f(\mathrm{mod}2\pi) = 2\pi(f - n)$, where f is the frustration index (or the fraction of a flux quantum enclosed in the unit cell) given by $f = \mathbf{H}a^2/\Phi_0$, and n is an integer (see [4] for the

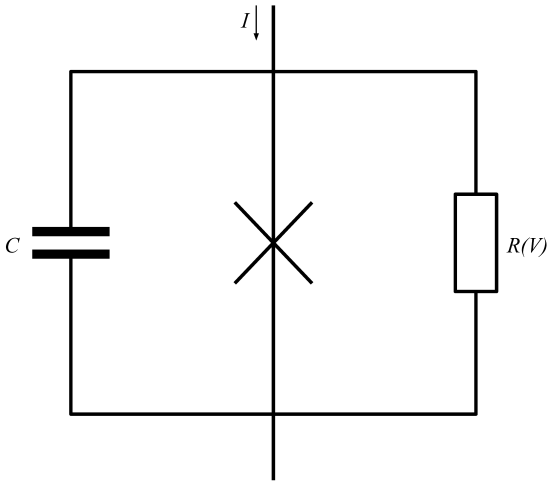

Figure 1.3.: The equivalent circuit of a Josephson junction, using a shunt resistor and capacitor

full calculation). Then for zero applied magnetic field and lattice spacing of a, the array is in the ground state ($f = \mathbf{H} = n = 0$) if the phase differences across the plaquettes are zero, and the energy of the array can be written as a sum of all single-energy plaquettes:

$$E = E_{\mathrm{J}} \sum_{\mathrm{array}} (1 - \cos \Delta\phi_i) \tag{1.25}$$

In such a scenario, the Josephson junction array becomes a physical realization of the XY-model[40].

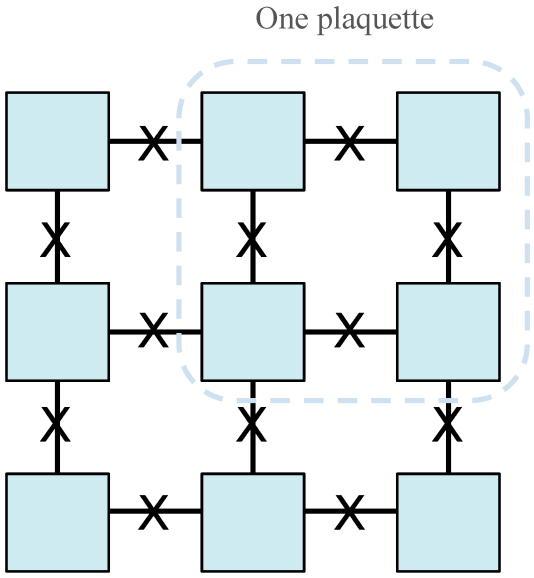

Figure 1.4.: Josephson junction array. The blue squares represent the superconducting islands, who are connected by weak links as represented by the lines with X's through them.

When a perpendicular magnetic field is turned on, the Pearl length discussed in the section on two-dimensional superconductors will also play an important role in Josephson junction arrays. The Pearl length is the length to which a superconductor screens magnetic fields, and in a Josephson junction array it depends on the critical current as

$$\lambda_\perp = \frac{c\Phi_0}{8\pi^2 I_c} \tag{1.26}$$

As long as the radius of the array ($R \gg a$) is much smaller than the screening length, screening effects can safely be ignored because the magnetic field is uniformly everywhere. However if the screening length is on the order of the lattice spacing, screening effects must be accounted for[4]. At this length scale the magnetic field will penetrate the array as a vortex lattice, and due to the periodic nature of the array the vortices will naturally find the lowest energy positions and be 'pinned' there [40]. The vortices repel one another, so the lowest energy positions are the ones in which the vortices are as far apart as possible. The vortices are located in the center of every other plaquette and the phase differences over the junctions in that plaquette are each $\pi/2$. From there, it can be understood that the fully frustrated array has a frustration index of $f = 1/2$, meaning that one-half of all unit cells contain a vortex[4], forming a checkerboard arrangement. More vortices cannot penetrate the array without causing a phase transition.

The array undergoes a BKT transition, and above T_{BKT} there will be an equilibrium amount of free ('unpinned') vortices which contribute to the linear resistance seen in the IV-characteristic (see figure 1.2). At zero-temperature (and zero field) all the phases in the array are aligned, but above zero temperature there can be no long range order due to thermal fluctuations in the alignment of the phases. It turns out that not only are single vortices excited by the thermal fluctuations but as predicted by BKT, vortex-antivortex (vortices of opposite sign) pairs will also be excited [19]. And since the energy of a single vortex is $E = \pi E_J \ln[R/a]$, which increases logarithmically with system size, it costs too much energy to form single vortices at low temperatures. It costs less energy to form vortex pairs whose energy cost increases only by the distance between vortices. So below the BKT transition temperature, vortex pairs are created who travel away from one another with increasing temperature until T_{BKT} is reached and one by one the bound pairs become free vortices [40]. At non-zero fields, the story is more complicated, however it has been experimentally observed that at integer levels of frustration, the array undergoes the same BKT transition as at zero frustration [42].

In the quantum regime, so at temperatures less than T_{BKT}, the charging energy becomes comparable to the coupling energy. This allows the charge on each superconducting island to be well-defined. And because the charge Q and the phase $\Delta\phi$ are conjugate variables, the phase is now uncertain. This leads to delocalization of the vortices and ultimately to frustration-dependent magnetoresistance. Studies have shown that there is a superconductor-insulator transition for certain frustrations (applied magnetic fields), where the sample resistance spikes from zero to a value three orders of magnitude higher [43]. At some frustration values

dR/dT is negative, indicating an insulating phase. And at others dR/dT is positive indicating an intermediate metallic state, much like the anomalous metal phase discussed previously. Additionally, the crossover point occurs at a value not far from the quantum of conductance, as seen in other anomalous metal studies[40]. Because Josephson junction arrays display the same features of the anomalous metal phase while being excellently tunable devices, they make an obvious choice of platform for further study of the anomalous metal phase.

The superconductivity of Josephson junction arrays can be coupled to a two-dimensional electron gas, and then a gate can be used to adjust the carrier density in the 2DEG. In this way, the superconductor to insulator transition can be stimulated. This creates a highly flexible platform for conducting experiments in the anomalous metal regime. Studies using this platform have shown repeatable results demonstrating the hallmarks of the anomalous metal phase, for example in [44], [29], and [45]. The promise of this platform has lead to the development of this thesis project. The experimental device developed in this thesis is structured as shown in figure 1.5. There are two microwave waveguides, one on either side of a Josephson junction array (blue grid). The array has a top gate (yellow) covering the entire array made from aluminum which is biased via a separate voltage source, V_G, used to tune the carrier density in the 2DEG located below the array. The four-probe resistance can be measured with the two voltage probes connected to the bottom of the array. The array itself is patterned on top of a semiconductor heterostructure, whose layers are shown in the stack up in figure 1.6. More information on this device is covered in section 5.

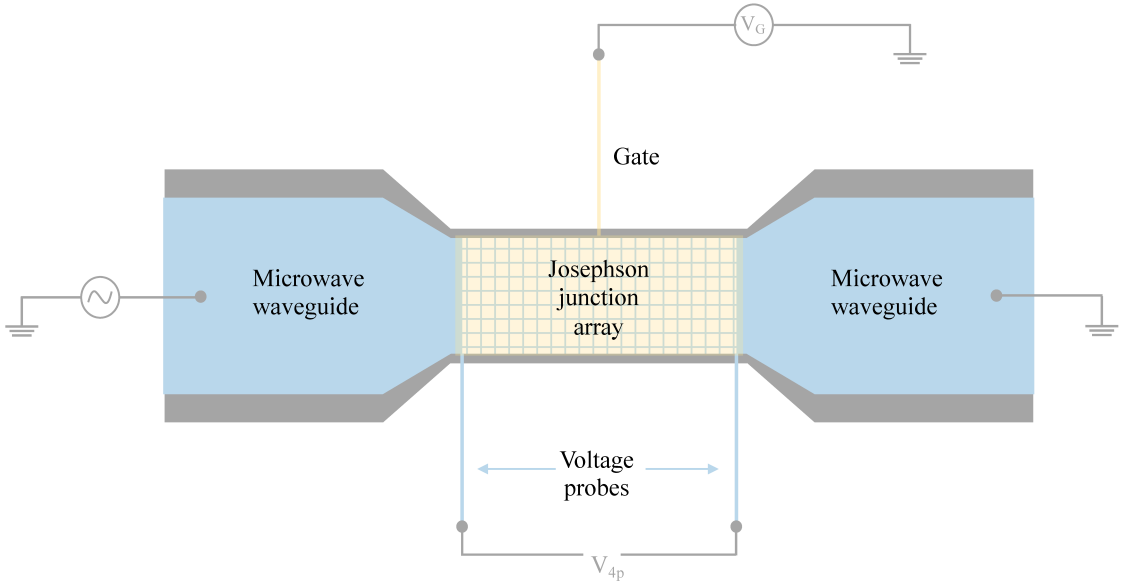

Figure 1.5.: Schematic of the device design. V_{4p} is the voltage measured for four-probe resistance measurements and V_G is the applied gate voltage.

While there have been many studies of the anomalous metal with this platform, so far there have been no publications characterizing the noise in this system as the superconductor to insulator transition is stimulated. The goal of the remainder of this thesis is to explain the steps taken toward preparing an experiment that will answer the question of how noise in

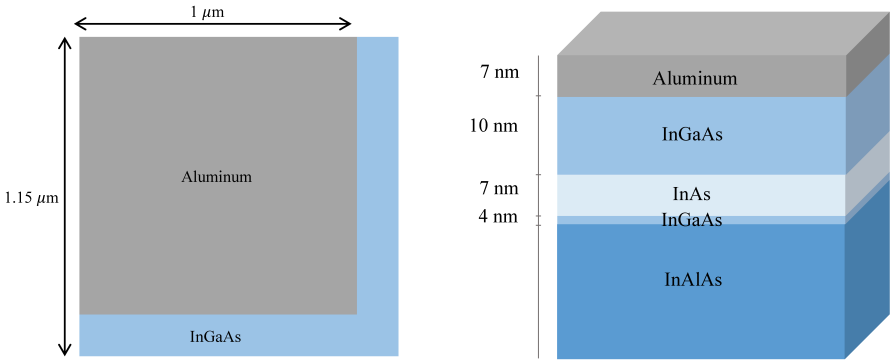

Figure 1.6.: On the left: the unit cell of the Josephson junction array. On the right: the stack-up of the layers in the device.

the anomalous metal behaves.

2. Experimental Methods

In this chapter, the individual pieces of the experiment will be presented and explained, to give an understanding of the experimental side of the project. This project was primarily supervised and carried out in the group of Prof. Andrew Higginbotham at IST Austria. As an overview, the Josephson junction array mentioned in the introduction is fabricated using nanofabrication techniques on an indium phosphate substrate chip. This chip sits on a gold-plated copper 'bracket', and is electrically connected to a printed circuit board. The whole package is then connected to a filter board and installed into a 'puck'. The puck is then loaded into a dilution refrigerator, where it will be measured at a temperature of about 20 mK. The measurement chain was customized for this experiment, from the design of the printed circuit board and bracket to microwave circuit elements inside the refrigerator.

2.1. Nanofabrication

Nanofabrication is a collection of techniques for creating structures at the nanoscale. The progress made in solid state physics since the last century has largely been made possible by developments in nanofabrication techniques. Superconducting quantum devices such as the Josephson junction array device used in this project typically go through several stages in the fabrication process. These steps take place in a cleanroom to reduce the chance of contaminating the sample at any stage.

The chip is created with a semiconductor heterostructure grown by our collaborators, the group of Javad Shabani at New York University. They grow the semiconductor heterostructure on a semi-insulating indium phosphate substrate. There are four epitaxially grown layers to the semiconductor heterostructure, from the bottom up: an InAlAs buffer, 4 nm of InGaAs, 7 nm InAs, and 10 nm InGaAs. A quantum well is formed in the 7 nm InAs layer, between layers of InGaAs. Once the substrate and semiconductor heterostructure have arrived, the superconducting device made of aluminum can be created on top.

Cleaning

The first step to fabricating the device is to clean the substrate very well. The chip is ultrasonicated in a bath of first acetone, then DMSO (dimethyl sulfoxide), then isopropanol (IPA). The ultrasonicator uses ultrasound waves to agitate the liquid in a glass beaker, cleaning the surface of the chip. Using three different chemicals to clean the chip ensures that spurious materials of differing chemical makeup will be removed from the chip.

Spin Coating

Next, the chip is placed in the spin-coating machine. This is the most efficient way to evenly and homogeneously coat the surface of the chip with an electron beam resist. The chip sits on a small rotating platform at the center of the spin-coating machine, and is held in place by vacuum. For static deposition, the resist is then squeezed with a pipette onto the chip. The spin-coating machine is then turned on and will spin the chip rapidly for a number of cycles until the resist has been evenly spread over the surface of the chip. In dynamic deposition, the resist is deposited onto the chip while it is spinning. Multiple rounds of spin coating can occur, to achieve a desired thickness of the resist. The resist, usually PMMA (polymethyl methacrylate), is needed to make a mask or pattern on the chip. It is the reaction medium that will be altered after interaction with the electron beam in the next step. A positive resist (low doses of PMMA) will be removed after exposure to the electron beam, and a negative resist (high doses of PMMA) will remain after exposure[46].

Electron Beam Lithography

The next step is to 'develop' the resist by exposing it via electron beam lithography (EBL). EBL is the process of drawing a specific pattern into a resist-covered substrate. A focused beam of electrons is radiated down with a resolution of about 10 nm, enabling the creation of structures on that scale. If the resist used was positive resist, the electron beam breaks some of the bonds between molecules in the PMMA, leaving molecules of lower weight behind that can then be washed away in the next step. If the resist used was negative, the exposure to the electron beam makes the bonds of the polymer in PMMA less soluble, so that only the unexposed sections are washed away. EBL is a direct-write technology, in contrast with other lithography processes that require use of specially patterned masks that cover the whole chip. This makes it more versatile and customizable. The pattern can be designed in an autocad software program and then is loaded into the EBL machine as a .dwg file, and then the EBL follows the pattern.

After exposure by EBL, the chip is placed in a solution of IPA and de-ionized water. This solution 'develops' the pattern by washing away the exposed (positive resist) or unexposed (negative resist) resist. For the Josephson junction array device, a positive resist is used, and after the development step, there will be suspended islands of PMMA for the aluminum to be evaporated onto in the next step.

Evaporation

For the growth of aluminum, special care has to be taken that the chip is not exposed to air during the growth process because it reacts very quickly with oxygen. After development of the device pattern, the chip is loaded into the UHV evaporator (ultra high vacuum) and then the chamber is pumped down to very low pressures. Aluminum is then deposited onto the chip to form the Josephson junctions and any other contacts. The PMMA will be removed, and the weak links between junctions will be left behind. Any excess aluminum is removed

by etching. The ground plane of the device (titanium and niobium) is deposited in the UHV evaporator as well, and any excess Ti/Nb is removed by liftoff in acetone.

Now the chip is ready to be used for experiments. The chip fabrication process takes about a week, as some of the steps mentioned above can take hours such as the EBL step. The chips in this project were manufactured by PhD student Duc Phan of our research group. The next step is to connect the chip with the printed circuit board.

2.2. Printed Circuit Boards

Printed circuit boards (PCBs) are the interface between the sample (on the nanofabricated chip) and the measurement devices (such as vector network analyzers, spectrum analyzers, current and voltage sources/meters, etc). They determine what experiments can be performed, and protect the chip while it is being measured. A PCB is a sandwich of conducting and insulating layers, with thin metal 'wires' directing current around the PCB. Signals are sent into a port on the PCB, and are directed through the PCB to another port on the board, and then could be sent to the sample and then back out of the PCB again. Both sides of a PCB can be used and be connected to one another through the use of 'vias' - holes covered in conductive metal to transfer a current from one layer of the PCB to another. They are highly customizable and versatile and there are many circuit elements that can be added directly to the PCB such as capacitors, resistors, inductors, transistors, and diodes to form circuits that will perform as desired. PCBs are usually designed using an autocad-like software on the computer, and then the designs are sent to a manufacturing company.

Care must be taken to design the PCB according to the specific needs of a project. If microwave or RF range signals are expected to be used, a strip line or microstrip can be formed on the PCB to allow high frequency signals to pass but it is important to design the dimensions such that the impedance of the line is close to $50\,\Omega$. At RF frequencies, the capacitance and inductance of the conductors in the PCB itself may become a significant concern, leading to unwanted resonances in the output frequency spectrum.

The chip will typically be attached to some kind of metal bracket with silver paste or vacuum grease, and then the PCB with a chip-sized hole cut out will be placed over top of the chip. The PCB is attached to the bracket with screws. The chip is then electrically connected to the PCB via wire bonds. A μm scale wire is attached to the PCB on one end, and to the chip on the other end. This is done with a tool called a wirebonder outside of the cleanroom after the nanofabrication process is complete. Depending on the design of the chip and the PCB, wires can be bonded from the microwave line on the PCB to a coplanar waveguide on the device, or a wire could connect two bond pads across the device to the PCB to read out DC voltage. Often the chip's ground plane will be bonded to the ground plane of the PCB to ensure that everything shares the same ground. Importantly, wire bonds can be a source of significant unwanted inductance, and it is best to design the PCB and chip to minimize

the length of these wires.

Once the PCB and the chip are set up they are ready to be placed into the puck, the canister that goes into the dilution refrigerator and connects the sample to the wiring inside.

2.3. Dilution Refrigerators

2.3.1. Working Principle

The dilution refrigerator is the best way to cool down a sample to the lowest currently attainable temperatures. They are used in all kinds of low temperature physics, from quantum computing to the search for Majorana fermions. There are two main categories of dilution refrigerators: the slightly older models are 'wet' fridges that use cryogenics in the cooling process, and the more modern fridges are 'dry' meaning that they get cold without having a liquid helium bath at any of the stages inside the fridge itself and are a closed loop system. Other methods of doing low temperature physics such as using a dewar of liquid nitrogen or liquid helium are cold enough for some kinds of superconductivity research, but temperatures on the order of 10 mK or less are necessary to do some kinds of research on quantum mechanical effects. Dilution refrigerators offer a convenient and reliable solution to reach these low temperatures.

Modern 'dry' dilution refrigerators are made of several stages, each of which is sitting at a different temperature. There is a 70 K plate, 4 K plate, a 'still' plate at about 700 mK, a 'cold' plate at about 100 mK, and the mixing chamber plate at about 10 mK. The pre-cooling loop connects the bottom three plates and cools them down over a period of about seven hours from room temperature to about 10K by letting a small amount of helium mixture to run through the loop. After this the fridge is brought down to about 2 K with a pulse tube cryocooler. To limit the effects of vibrations produced by the pulse tube, they are decoupled from the lower three plates via copper braids. At the final stage, the dilution refrigerator uses two isotopes of helium to derive its cooling power, a mixture of ^{3}He and ^{4}He. Around 2.17 K the ^{4}He begins to transition to a superfluid, and the dilution process can begin. The final steps of the cooling process take about two hours to reach the base temperature of the fridge.

^{3}He particles are fermions which obey Fermi-Dirac statistics and at low temperatures behave like a Fermi liquid. They do not form a condensate due to the Pauli exclusion principle. In contrast, ^{4}He particles are bosons which do form a Bose-Einstein condensate under 2.17 K. They start to become a superfluid and exist in a two fluid state of normal and superfluid, while the ^{3}He remain in a normal state. The temperature continues dropping due to the heat exchangers between the three experimental plates. Around 1 K nearly all of the ^{4}He particles are in the superfluid state, with zero entropy or viscosity. If the mixture has at least 6.6% ^{3}He, there will be a tri-critical point at just under 1 K below which phase separation occurs. Here, the mixture separates into a ^{3}He-rich (concentrated) and a ^{3}He-poor phase (diluted) [47]. Because ^{4}He is heavier than ^{3}He, the concentrated phase floats to the top. There is an

entropy difference between the concentrated and dilute phases, so as the mixture transitions endothermically to the concentrated phase heat will be extracted. 'Hot' ^{3}He then flows out of the mixing chamber to the still stage where a heater boils off the ^{3}He and pumps it through the cooling loop. The still stage is named for its role in distilling the ^{3}He from the ^{4}He. The gaseous ^{3}He is then pumped back around to the still stage on the other side where it enters a constriction in the pipe called an 'impedance' which ensures the pressure is high enough to force the ^{3}He to condense back into a liquid. The returning ^{3}He is once again cooled by the heat exchangers before repeating the dilution process again. This continues, and depending on several factors (the amount and type of things mounted on the experimental stages, leakiness of the fridge, thermal isolation, etc) a base temperature will be reached that is maintained by the dilution process.

At such low temperatures, a normal thermometer will not accurately measure the temperature. Metallic resistance thermometers measure a positive temperature derivative and can be used between $\sim$1 K and room temperature. When calibrated, they give a very accurate measurement of temperatures in this range by recording the resistance. Below $\sim$1 K, semiconductor-like resistance thermometers must be use. They measure a negative temperature derivative and while they are much more sensitive than metallic thermometers at low temperatures, they are less sensitive at temperatures above $\sim$70 K[48]. As a result, each stage of the fridge has a thermometer, and depending on how cold each stage gets, a semiconductor-like thermometer might be added to that stage. Both are needed to accurately measure the temperature of each stage at every temperature. At the mixing chamber stage of the fridge used in this project there is a Cernox thermometer as well as a RuO_2 thermometer. The final piece of the measurement setup is how to send a signal to the device and read back the response.

2.3.2. Microwave Readout Chain

A microwave measurement often begins with a vector network analyzer (VNA). In this measurement setup the signal leaves port one and travels through a coaxial cable to the top of the fridge. On the way down to the sample the signal winds through the various temperature stages via stainless steel coaxial cables, passing some amount of attenuation at each stage. The total attenuation in the fridge used in this project is 50 dB, allowing the temperature seen by the sample to be about 23 mK at the mixing chamber. The calculation to arrive at this figure is included in the appendix A. Once the signal reaches the bottom of the fridge there are two options: it either passes into the puck and through to the PCB, and from the PCB across the sample and then back up through a circulator. Otherwise if the measurement is in reflection setup, the signal will divert at the mixing chamber stage to a circulator, and then head down to the puck and the PCB and the sample, before returning back up through the same circulator (but it will exit through another port on the circulator). From the output port of the circulator the signal will pass through another circulator and then up through the cold and still plates to reach the amplifier on the 4 K plate. From there it passes through the next two plates and out of the top of the fridge. Then, depending on the goal of the

measurement it either returns to the VNA or to some other instrument. A schematic of the wiring inside of the fridge is shown in figure 2.1. As an example, a signal may be sent down line 7, pass through the circulator to the sample, reflect back off the sample, and then pass back out through line 8.

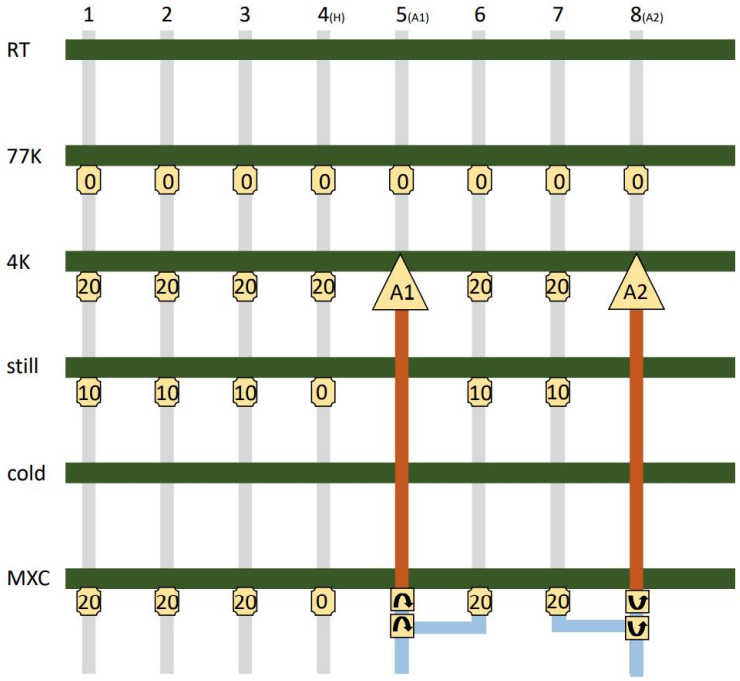

Figure 2.1.: Diagram showing the different microwave lines in the fridge, the attenuation at each, and different circuit elements that are installed. Blue lines indicate copper coaxial cable, gray lines indicate stainless steel coaxial cable and red lines indicate superconducting coaxial cable.

2.3.3. Thermalization Considerations

The thermalization of the fridge and the signal is a primary concern. Many things can affect the thermalization of components installed in the fridge. The thermal conductance for all materials is a function of temperature, so components installed at higher temperature stages in the fridge warrant different thermalization considerations than components installed at the mixing chamber. Solder in its many forms is one of the best thermal conductors, so components soldered onto the PCB will likely be excellently thermalized to the rest of the board, and the same goes for other soldered wires in the fridge such as the wires connecting the power supply for the amplifier to the amplifier[48].

The thermal contact of the chip to the sample holder must also be optimized. The thermal conductance has been experimentally found to increase linearly with pressure, so to increase the heat conductance between two solids a lot of pressure has to be applied. A chip, however, cannot be pressed against the sample holder without damaging the delicate nanofabricated structures, nor can it be soldered to the sample holder. In the case of low pressure applications like this, the best way to ensure thermalization is to apply either vacuum grease or silver

paste to the sample holder before gently setting the chip on top. This doubles as an effective way to glue the chip to the sample holder. Additionally, the chip has a relatively large surface area with which to make contact with the sample holder, a case for which grease is well-suited. It would be logical to think that adding grease to any contact, even if high pressure can be applied, could increase the thermal conductivity, but in fact there is a tipping point at which grease no longer helps[48]. At high enough pressures, or low enough temperatures, vacuum grease will actually decrease the thermal conductivity of the interface. At this point it is better to simply bolt or otherwise fasten them together. Which is the case for the screws that fasten the PCB to the sample holder and the sample holder to the puck. They achieve high enough force, at low enough temperature, that the only way to increase thermal conductivity is to coat them in gold plating before screwing them together. This is also true for the circulators installed at the mixing chamber stage of the fridge. However, the amplifiers installed at the 4 K plate are at a high enough temperature that it again makes sense to add grease before screwing them into the fridge. The calculations to determine whether or not to grease the interface before installing a component in the fridge are relatively straightforward, an example is given in appendix B.

It is also important to consider how the signal arrives at the top of the fridge from the sample in terms of thermal noise. The temperature difference between different stages is abrupt, and to avoid adding large amounts of thermal noise before the signal can be amplified at the 4 K stage by the amplifier, superconducting coaxial cables are used. Every connection between components on the same temperature stage can be done with a regular copper coax, but any cable that transverses temperature stages must be made from a niobium-titanium superconducting coaxial cable (NbTi has a critical temperature of about 9.7 K). Above the amplifier and before reaching the sample, stainless steel coaxial cables are used because once the signal has been amplified, any added thermal noise will be minuscule in comparison. Before reaching the sample the calculated added noise due to the attenuators has already been accounted for.

2.3.4. DC Measurements

DC transport measurements are in many ways simpler than microwave measurements. There are established methods for reading out the voltages and currents and resistances using a breakout box, a digital multimeter, and a lock-in amplifier and the measurements are rather straight forward. Dealing with amplifiers and whether the circuit elements are all in-band is simply not an issue. The abovementioned concerns about thermalization are also much less pertinent. A wire travels from the front of the breakout box through a connector into the top of the fridge, where it meets a line that goes directly down to the sample puck. From there the line is plugged into the PCB, and along the PCB a wire travels to the correct bond pad, which is then connected to the sample via a wire bond. So long as all the cables are in good shape, plugged in, and appropriately grounded, the current will flow and measurements can be taken.

3. PCB Design and Testing

The overarching goal for this project was to design an experiment to measure the noise signature of the anomalous metal phase. From the beginning, it was clear that the previously installed measurement apparatus in the lab would not be sufficient for this goal. To achieve the intended measurement it would be necessary to design a new PCB, sample holder, microwave measurement chain, and measurement circuit. The steps taken to make progress in building up the experiment are explained in more detail below.

3.1. Initial Calculations

To begin, we had to decide on the frequency at which to conduct the microwave measurements. The considerations in choosing a frequency were that we wanted to be at or near the quantum limit given by $h\nu \sim k_\mathrm{B}T$, so whichever frequency we chose would be associated with a temperature. This temperature needed to be easily accessible with the dilution refrigerator involved in this experiment. Additionally, we wanted to minimize the temperature, to avoid adding any extra thermal noise that could obscure the 'good' noise. Lastly, while there are many RF circuit components in the 4-8 GHz band, there are fewer at higher and lower frequencies and we needed to be sure that there would be components available in whichever band we chose. The sweet spot was determined to be somewhere around 1 GHz, which corresponds to a temperature of about 50 mK according to

$$h\nu \sim k_\mathrm{B}T \tag{3.1}$$

$$h \cdot 1\,\mathrm{GHz} \sim k_\mathrm{B} \cdot 50\,\mathrm{mK} \tag{3.2}$$

We are able to reach this limit because our fridge routinely reaches temperatures of around 20 mK. And because all required RF circuit elements in the 1 GHz frequency range are commercially available, the criteria are fulfilled. The 4-8 GHz frequency band (∼200-400 mK) was identified as a back-up option in case of unpredicted delivery problems.

The next calculation involved making sure that the power dissipated in the circuit stayed constant over the frequency range that we are using. With the wrong circuit elements or sample parameters, we could risk the power being reflected or entirely dissipated before reaching the load resistor Z_L. This would mean that the power (the noise power) would not be measurable. For this we needed a circuit model to represent the different sources of resistance and capacitance in the measurement chain. This circuit model is shown in figure 3.1.

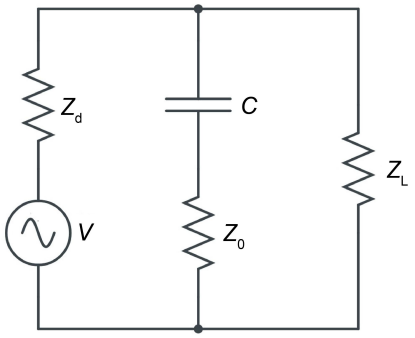

Figure 3.1.: Model of the measurement circuit using impedances. Z_d represents the device impedance, Z_L represents the load impedance, and Z_0 is the $50\,\Omega$ impedance of the circuit. C is the capacitance generated by the gate on the sample.

The analysis of the circuit is supported by section 4.1 and 4.2 of David Pozar's *Microwave Engineering*[49]. To begin, we recognize that this circuit is simply a voltage divider with a load on the second resistor. The rule for calculating the output voltage on a loaded voltage divider is

$$V_\mathrm{out} = V_\mathrm{in}\frac{Z_\mathrm{L} \parallel (Z_0 + X_\mathrm{C})}{Z_\mathrm{d} + Z_\mathrm{L} \parallel (Z_0 + X_\mathrm{C})} \tag{3.3}$$

where X_C can be represented as $X_\mathrm{C} = 1/i\omega C$. Since $Z_0 + X_\mathrm{C}$ is in parallel with the load resistor, the resulting impedance is calculated in the form $\frac{1}{R_{\mathrm{a+b}}} = \frac{1}{R_\mathrm{a}} + \frac{1}{R_\mathrm{b}}$:

$$\frac{1}{Z_\mathrm{L} \parallel (Z_0 + \frac{1}{i\omega C})} = \frac{1}{Z_\mathrm{L}} + \frac{1}{(Z_0 + \frac{1}{i\omega C})} = \frac{Z_0(1 + i\omega C)}{1 + 2i\omega C Z_0} \tag{3.4}$$

now combining equation 3.3 and 3.4 into one equation we arrive at a solution for V_out

$$V_\mathrm{out} = V_\mathrm{in}\frac{Z_0 + i\omega C}{Z_\mathrm{d} + 1 + i\omega C Z_0} \tag{3.5}$$

Assuming that we know the values for V_in, Z_d, ω, and C, we can then use this equation to calculate the output voltage of the circuit. Ultimately, we would like to know what the power delivered to the load resistor is. However, because this circuit has imaginary components (as in the case of lossy transmission lines), the expression for complex power delivered to a load is[49]

$$P = \frac{1}{2}\mathrm{Re}\left[\frac{|V_\mathrm{out}|^2}{Z_\mathrm{L}^\star}\right] \tag{3.6}$$

which has been calculated from the difference between the power of reflected and incident power waves. To calculate the square magnitude of the output voltage we use $|V_\mathrm{out}|^2 = \mathrm{Re}\,[V_\mathrm{out}]^2 + \mathrm{Im}\,[V_\mathrm{out}]^2$. After some algebra we arrive at the following expression for $|V_\mathrm{out}|^2$

$$|V_\mathrm{out}|^2 = \frac{V_\mathrm{in}^2(Z_0^2 + \omega^2 C^2)\left[(Z_\mathrm{d}+1)^2 + 4\omega^2 C^2 Z_0^2\right]}{(Z_\mathrm{d}+1)^2 + 8(Z_\mathrm{d}+1)^2\omega^2 C^2 Z_0^2 + (4\omega^2 C^2 Z_0^2)^2} \tag{3.7}$$

From here it is straightforward to calculate the power delivered to the load by plugging in the values for the variables. Calculations for various parameter choices are shown in the

appendix C. The device parameters used in these calculations were modeled based on the devices used in [29], and [45]. We intended to fabricate similar devices, and as such needed to design an experimental setup that would work for the parameters of such a device. The calculations showed that indeed for such a device, over the frequency range we chose, the power delivered to the device remains sufficiently high.

3.2. Characterizing Electronic Properties of the PCBs

The first PCB

Previously the lab had been using one kind of PCB that didn't have very many DC bonding pads (meaning that only one or two devices could be manufactured on the same chip), and didn't allow for the possibility to measure microwave and DC signals at the same time. In the context of this thesis a new PCB had been designed and ordered that had forty DC bond pads, which would give much more flexibility for the design of samples. This PCB can be seen in figure 3.2[1].

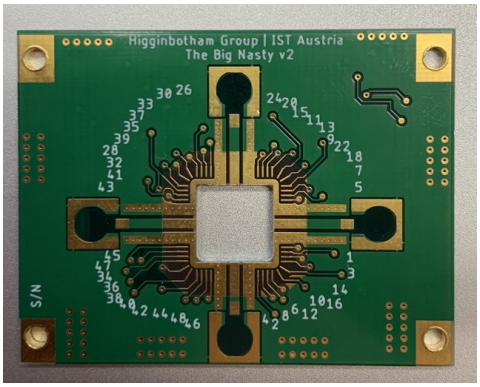

Figure 3.2.: The first version of the PCB.

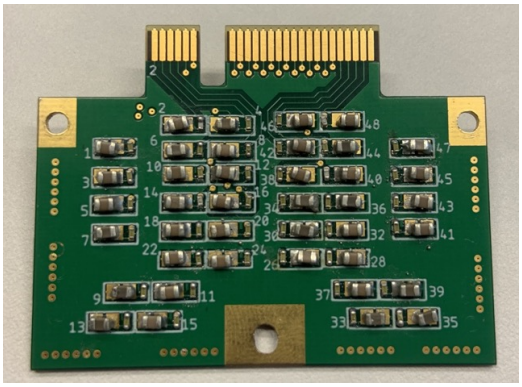

Figure 3.3.: The first version of the filter PCB.

The extra value of this PCB was that it could be connected to a filter PCB, where each line would include a low pass filter to get rid of unwanted high frequency signals, see figure 3.3. This re-design meant that a new sample holder had to be designed. The filter PCB would be attached to the sample PCB via a nano-D connector on the back of each PCB, and the two PCBs would then have to be connected to a sample holder so that the chip could sit in the pocket of the sample PCB (the pocket being the square at the center of figure 3.2).

This is achieved with a bracket that fits in between the two PCBs, so that the sample PCB could fit over the sample holder with the pocket in the right place, and then the filter PCB could be attached onto the back of the sample PCB, with a bracket of the right thickness in between them. The bracket alone is shown in figure 3.4, and in combination with the two PCBs in figure 3.5, where the sample PCB is the second iteration, which will be introduced

[1] All PCBs in this experiment were designed and ordered in coordination with the machine shop at IST Austria.

in the next section. The PCB can be further secured to the holder by screwing into the holes seen at all four corners of the PCB, and on the back there are two holes to screw the filter PCB into as well. There is an additional optional clamp not pictured to further secure the PCBs firmly to the bracket. The bracket was manufactured by the IST Austria Miba machine shop.

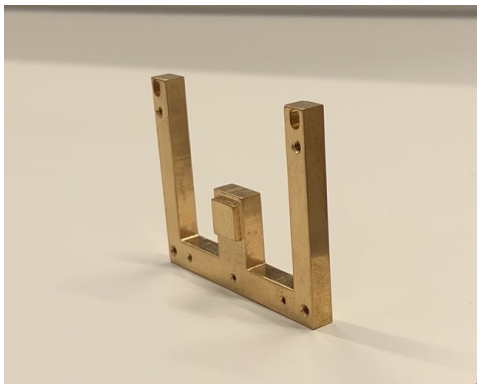

Figure 3.4.: Sample holder, material is copper with gold plating over top.

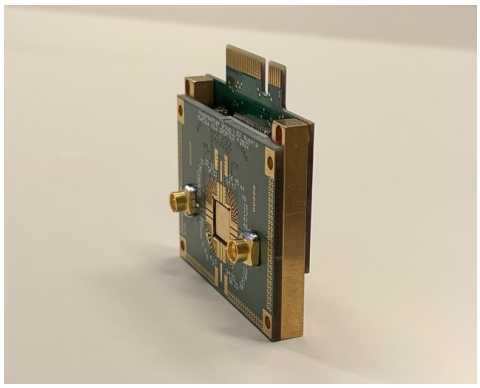

Figure 3.5.: Sample holder with both sample PCB and filter PCB attached.

With the sample holder bracket designed, it became time to test the PCBs to ensure both that there weren't any PCB-induced resonances in the frequency range of our experiment and that there was good transmission through the PCB (low insertion loss). It is generally difficult to calculate the exact transport properties because there are so many contributing factors (distance of lines away from one another, thickness of each layer, layout of the components, how large the ground planes are, etc.). There are often several iterations necessary. While testing these boards we found that there were errors in the numbering of the DC lines. We also found that the design of the SMP launchers (where the microwave connectors attach to the PCB) was improper. the middle gold strip did not extend deep enough into the middle of the SMP launcher and the SMP connectors couldn't get a good enough connection. The soldering pads on either side were also widened to allow easier soldering and better grounding for the SMPs. These two factors required us to design a second generation PCB.

The second PCB

The new PCB is shown in figure 3.6. The numbering scheme matches the breakout box. The design of the SMP launcher pads has been improved. The microwave transmission showed a smooth frequency dependence with little insertion loss over the frequency range we are interested in (less than 2dB of loss over 0-2 GHz). We also re-designed the filter PCB to increase the size of the capacitor-to-ground and resistor-to-capacitor connections as a precaution (shown in figure). These new PCBs are suitable for use in experimentation.

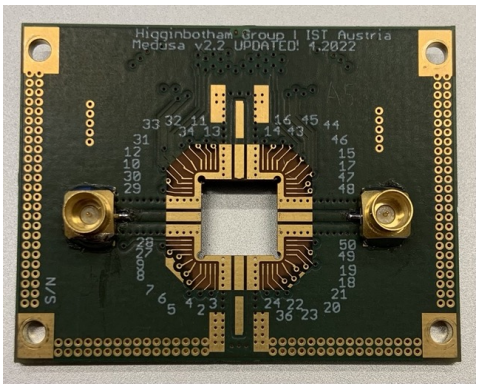

Figure 3.6.: Version two of the PCB, with updated numbering scheme and correctly designed SMP launchers.

The third PCB

Concerning the measurement chain for the experiment, it would be beneficial to include bias tees on the board, rather than as a separate circuit element or included on the chip itself. A bias tee is a circuit element with three ports, one port through which both high and low frequencies can pass, one through which only low frequencies can pass, and one through which only high frequencies can pass, and is shaped like a 'T' as shown in figure 3.7. This would be convenient for measurements because it ensures that the bias-tee is thermalized to the same temperature as the sample and requires much less space in the fridge. Additionally, this on-board bias tee will be highly tunable for different frequency range demands, without having to re-design the PCB (see section 3.3).

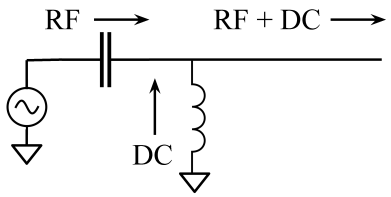

Figure 3.7.: Bias tee circuit element.

We therefore decided to modify the design and include bias tee circuit elements on the PCB. We performed tabletop experiments to determine the best inductor/capacitor combination to ensure proper working of the bias tee. Bias tees work in the typical 50 Ω transmission line setting, and the capacitance is chosen such that the impedance of the capacitor is much less than the characteristic impedance of 50 Ω

$$X_C = \frac{1}{\omega C} = \frac{1}{2\pi f} << Z_0 \tag{3.8}$$

and similarly the inductance is chosen so that the impedance of the inductor is much greater

than 50 Ω

$$X_{\mathrm{L}} = \omega L = 2\pi f >> Z_0 \tag{3.9}$$

The capacitance and inductance have been carefully selected as to avoid impacting the frequency range of interest through resonances and LC-tank circuit behavior. It is also important to note the self-resonance frequency (SRF) of the chosen inductors. An inductor's impedance reaches a maximum at the SRF and the inductance changes abruptly from positive to negative at this frequency. In other words, the inductor becomes a capacitor at the SRF and doesn't work as an inductor above that frequency. The manufacturer-specified SRF can be different from what is seen in practice, because the exact parameters of the PCB can change the overall resonant frequency.

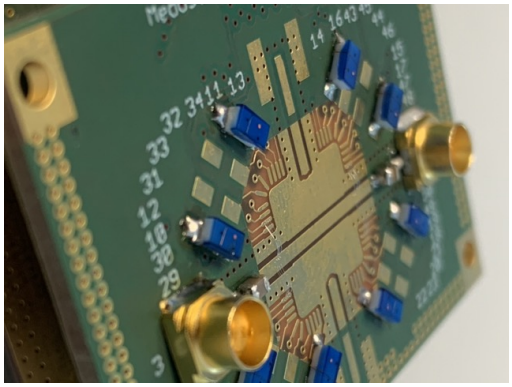

Figure 3.8.: The third iteration of the PCB, now with inductors (blue).

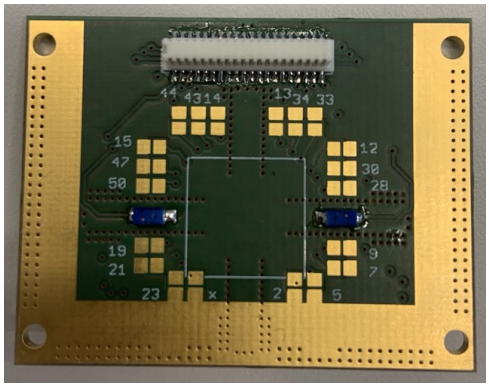

Figure 3.9.: The third iteration of the sample PCB, seen from the back.

We selected elements for the target frequency range of 0-8 GHz, particularly at 1 GHz and between 4-8 GHz. As starting parameters we chose 3.3 nH inductance and 47 nF capacitance[2]. The impedance of the capacitor at 1 GHz is about 3.4 mΩ, and at 8 GHz it is about 0.4 mΩ, which is much less than the characteristic impedance. The impedance of the inductor at 1 GHz is about 20 Ω, and at 8 GHz it is about 166 Ω. Although the inductance is low for the low range of the frequency that we are interested in, we performed tests to characterize the electronic properties of the board and establish a starting point.

The third iteration of the PCB is shown in figure 3.8. The inductors that make up the bias-tee on the microwave line are included on the back side of the PCB (see figure 3.9). In this way, the PCB can be customized to the desired capacitor/inductor combination, by soldering them onto the PCB and replacing them if no longer needed. A schematic of the third iteration PCB's circuitry is shown in figure 3.10. In the schematic, the filter PCB is included, in the form of resistors and capacitors on the lines, and the '...' represents the other fourteen bias tees on DC lines. The remaining DC lines route directly to the filter PCB. In this way, RF signals can be sent from VNA Port 1 across the device to VNA Port 2, and at

[2]The inductors used in this project are the 1206CS (3216) high temperature ceramic chip inductors from CoilCraft, and the capacitors are C0805C series 47nF capacitors from Kemet.

the same time DC signals can be sent from the breakout box to the device as well.

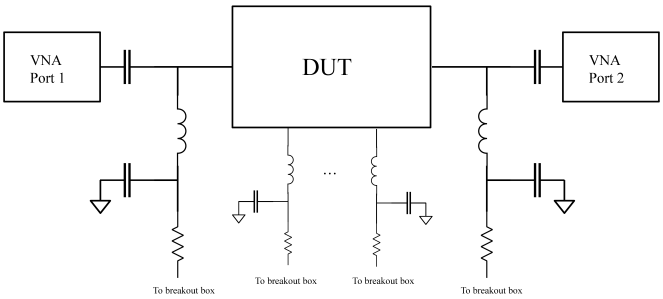

Figure 3.10.: Circuit schematic for PCB version three.

3.3. Optimizing Bias Tee Properties

The first PCB with 3.3 nH inductors and 47 nF capacitors had many unwanted resonances throughout the frequency spectrum when measuring the S21 magnitude with a VNA. The measurement setup consisted of a VNA, two coaxial cables, and the PCB itself as depicted in figure 3.11.

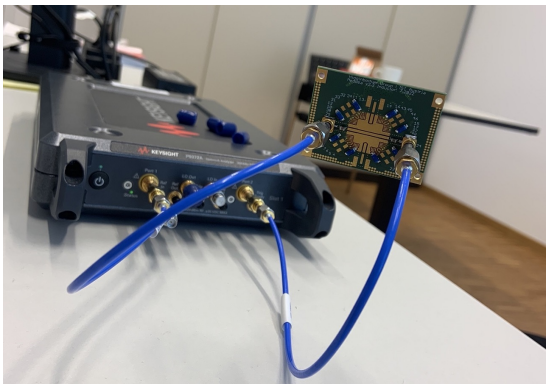

Figure 3.11.: The measurement setup for the tabletop tests.

We tested several combinations of inductors and capacitors to improve the impedance properties of the PCB. The initial tests concerned only the two inductors on the back of the PCB. We found that when the inductors were removed, the transmission spectrum became more homogeneous, as shown in figure 3.12.

This suggested that the resonances were related to the inductors. To confirm this hypothesis, we carried out similar measurements with the second iteration of the PCB and found a comparable improvement when removing the inductors (see figure D.1 in the appendix D).

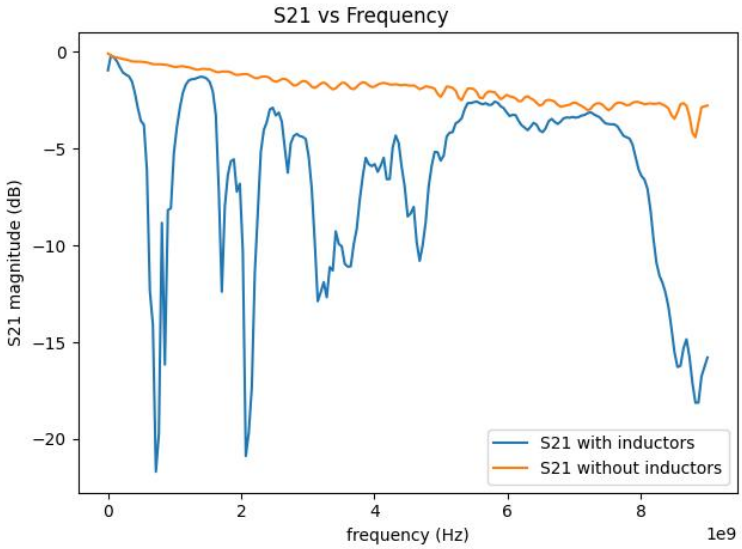

Figure 3.12.: S21 magnitude vs frequency plots for PCB version three, with and without inductors.

This indicates that the change of design of the PCB from iteration two to three has minimally impacted the PCB's 'ideal' transmission spectrum.

We suspect that the origin of the resonances lies in the impedance seen by the incoming RF signal as it approaches the inductors. Either the signal doesn't see the ground on the opposite side of the inductors, or the ground is too far away, and resonances could form in that space. To test this theory we added capacitors to the ground-side of the inductors on the back of the PCB, and then grounded the back side of the capacitors with wires, as seen in figure 3.13. This would cause the AC signal to see a large capacitance to ground on the opposite side of the inductors, and be prohibited from entering.

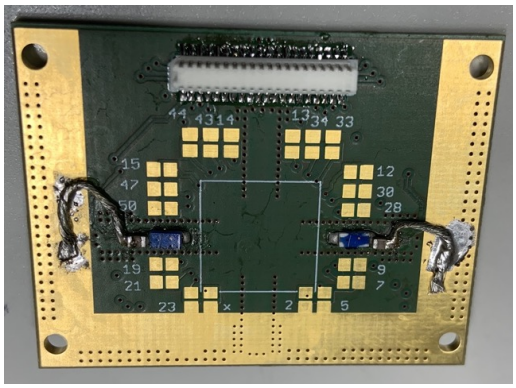

Figure 3.13.: The version three PCB with extra capacitors and wires soldered to the ground plane.

The S21 transmission of the modified PCB showed many fewer resonances than previously, as seen in figure 3.14. By optimizing the capacitance and inductance, the loss at low frequency

could be reduced. At high frequency there is an additional flat, low-loss region between 4.5-7.5 GHz. This is nearing the edge of the SRF region of the manufacturer's spec sheet for the inductors, but as the impedance of the inductors grows towards the maximum, the transmission spectrum appears to get rid of the extra resonances. Perhaps the decline in S21 magnitude after 7.5 GHz is due to the SRF of the inductors being reached, and the inductors no longer working properly.

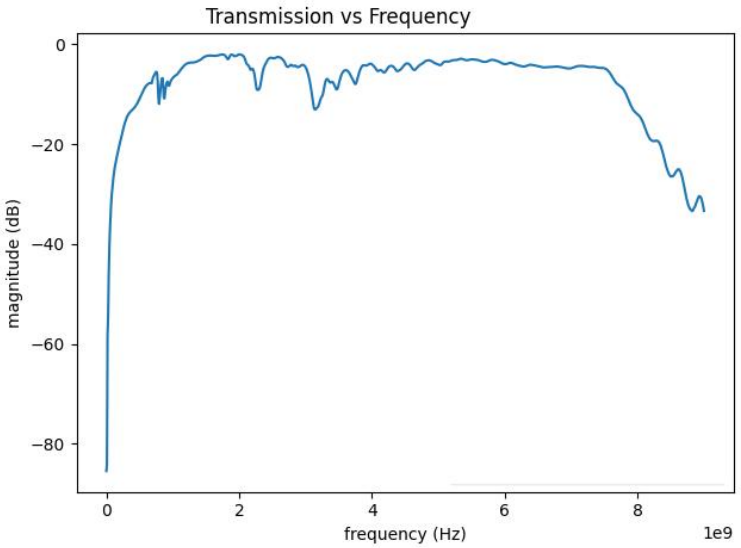

Figure 3.14.: S21 of PCB version three with extra capacitors and wires soldered to ground.

By experimenting with different capacitor values, we found that the roll-off of the S21 magnitude toward lower frequencies could be adjusted by the capacitance (see figure D.2 in the appendix D). We then investigated the DC bond pads. Sixteen of the DC lines also have bias tees on them. There are inductors soldered to eight DC lines as can be seen in figure 3.8. We used the four closest to the transmission line (the solid gold-colored strip running from one capacitor to the other) to wirebond from DC bond pad to the transmission line. This would investigate how the DC lines looked electrically. As shown in figure 3.15, the S21 magnitude with all four inductors wirebonded has many resonances, and is much noisier than what was achieved with the microwave bias tees in figure 3.14. So we soldered capacitors and wires to ground on all four inductors as seen in figure 3.16 and figure 3.17.

This did not have quite the same effect as when done on the microwave bias tees, as evidenced by the blue trace in figure 3.15. While there are fewer and weaker resonances once the capacitors and grounding wires are added, the resonance near 5 GHz increased in strength, and the overall spectrum has more resonances than the microwave-only case in figure 3.14. This behavior of the DC lines must have a different origin than what had caused the behavior on the microwave line, and we will investigate further in a fourth iteration of the PCB.

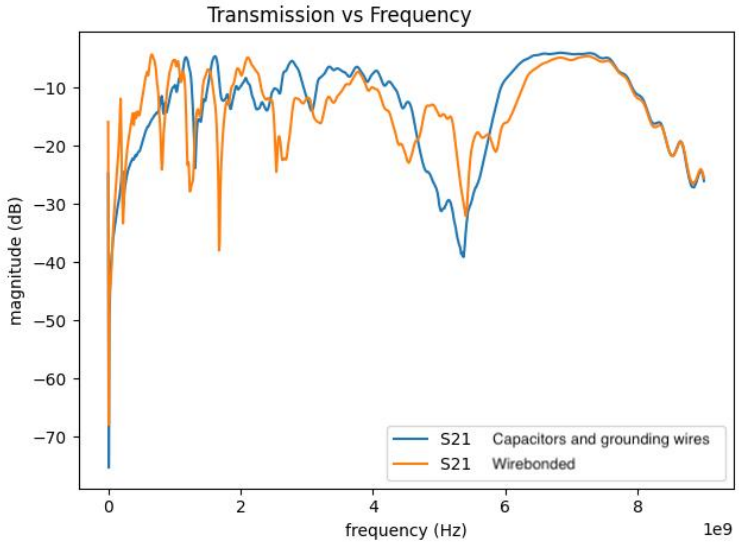

Figure 3.15.: Comparing the S21 of wirebonded DC pads to the transmission line with wirebonded DC pads plus soldered capacitors and grounding wires for PCB version three.

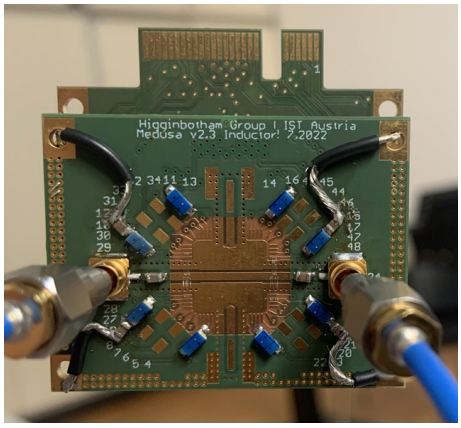

Figure 3.16.: PCB v3 with wirebonds from DC bond pads to the transmission line, and capacitors and grounding wires soldered to the DC bias tees.

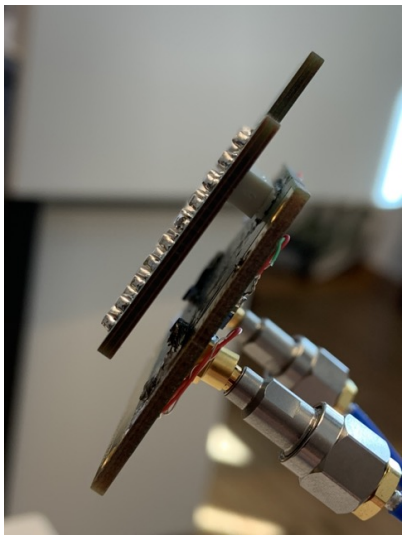

Figure 3.17.: PCB v3 from the side, with the filter PCB attached while being measured on tabletop.

The fourth PCB

We re-designed the PCB with capacitors to ground on the back side of all bias tees, microwave and DC, and better grounding to every line. The fourth version of the PCB can be seen in figure 3.18 and figure 3.19, where only a few of the inductors and capacitors have been soldered onto the board. The idea was that with proper grounding and solder pads for the new capacitors-to-ground, the S21 transmission for all bias tees will have fewer resonances and similar insertion loss as the second version of the PCB across the frequency spectrum.

This would help to clarify the behavior of the DC line bias tees. The new circuit schematic is identical to figure 3.10 except that now there are two capacitors in parallel between the inductors and resistors on each line, representing the new capacitor to ground from the inductor. After checking that the S21 transmission for the microwave still looked reasonable (figure D.3 in appendix D, low insertion loss and almost no low frequency resonances), we moved on to checking the DC lines.

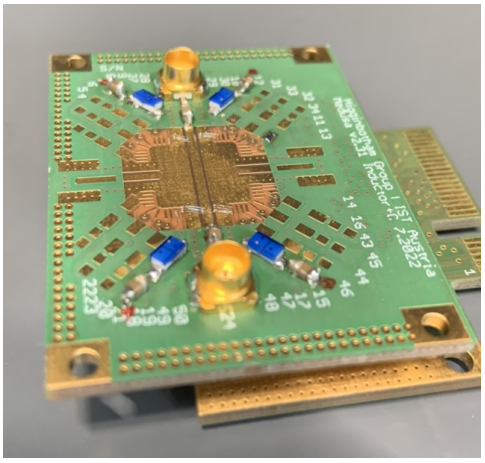

Figure 3.18.: The fourth iteration of the PCB, with capacitors to ground on all bias tees.

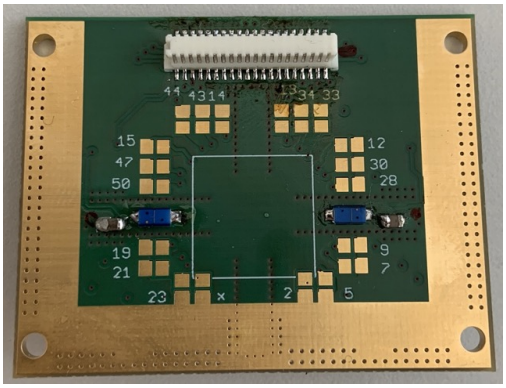

Figure 3.19.: The fourth iteration of the PCB, view of the back.

The DC lines spectrum had fewer resonances than before, see figure 3.20, though it did still have more than the microwave bias tee spectrum. There were a few noteworthy features: the roll-off as frequency goes to zero, and the two distinct dips around 4 and 7.5 GHz. The dips beyond 8 GHz are outside of the frequency band that we are interested in. To investigate the origin of the roll-off near zero frequency we removed all the inductors to test if the roll-off was still present, see figure D.4 in appendix D. The spectrum showed low insertion loss and no resonances before some high-frequency roll-off. We concluded that the capacitors are not solely responsible for impacting the low-frequency roll-off.

We then tested the influence of the wirebond connections. We systematically removed the wirebonds one at a time, and recorded the S21 after each removal, see figure 3.21. The blue trace has sixteen wirebonds total (four times on each pad). The orange trace has one bond on each pad. We then removed them one by one and recorded the S21 in between.

The low frequency roll-off is improved for fewer wirebonds. Simultaneously the resonance around 4 GHz reduced in frequency as wirebonds were removed. In contrast, the resonance at about 7.5 GHz, didn't change. This implies that the resonance at about 7.5 GHz is due to some intrinsic feature of the PCB, while the dip at about 4 GHz as well as the low-frequency roll-off are related to the wirebonds.

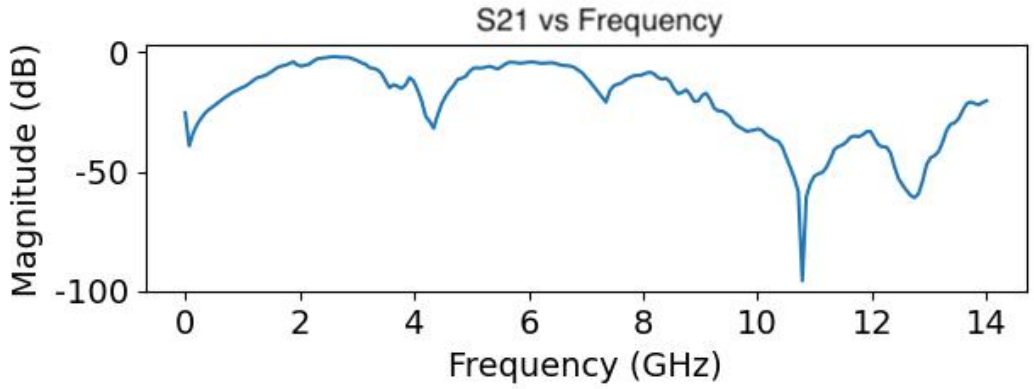

Figure 3.20.: S21 vs frequency for the DC lines on PCB v4. One wirebond connects each DC line to the transmission line.

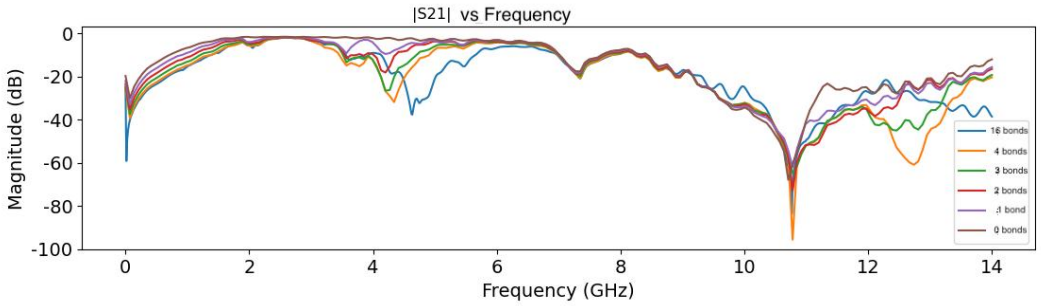

Figure 3.21.: Removing the wirebonds from the PCB one by one and recording S21 vs frequency at each stage. The first trace (blue) has four wirebonds on each DC pad (in total 16 wirebonds). Inductors are 3.3 nH.

Wirebonds can be a source of extra inductance, particularly when they are very long, as their inductance scales with their length. The wirebonds from the DC pads to the transmission line are rather long, and could add an appreciable amount of inductance. The wirebonds on the DC pads are in parallel with one another, so as they are removed, the inductance due to the wirebonds increases (as inductances in parallel with one another add as $1/L_{\mathrm{a+b}} = 1/L_{\mathrm{a}}+1/L_{\mathrm{b}}$). We observe that as the number of wirebonds decreases, the resonance at about 4 GHz decreases in frequency as well. This is aligned with the hypothesis that the wirebonds add inductance in parallel with one another. If this resonance is due to a tank circuit created by the inductors and capacitors and wirebonds, then as the inductance added by the wirebonds increases, the resonant frequency ($\omega_0 = 1/\sqrt{LC}$) should decrease, which is what we observe.

We then demonstrated control over the resonance by trying different inductors. We replaced the 3.3 nH inductors with 15 nH inductors. The 15 nH PCB has less roll-off at lower frequencies than the 3.3 nH PCB (see figure 3.22), and the dip due to the inductance of the wirebonds has moved down in frequency (see figure 3.23). As the inductance of the inductors increases, this inductance adds in series with the inductance due to the wirebonds, so an increase in the inductance should lead to a reduction in resonant frequency of the tank circuit. Additionally, the noisiness of the spectrum decreased with the 15 nH inductors. Now the areas on either

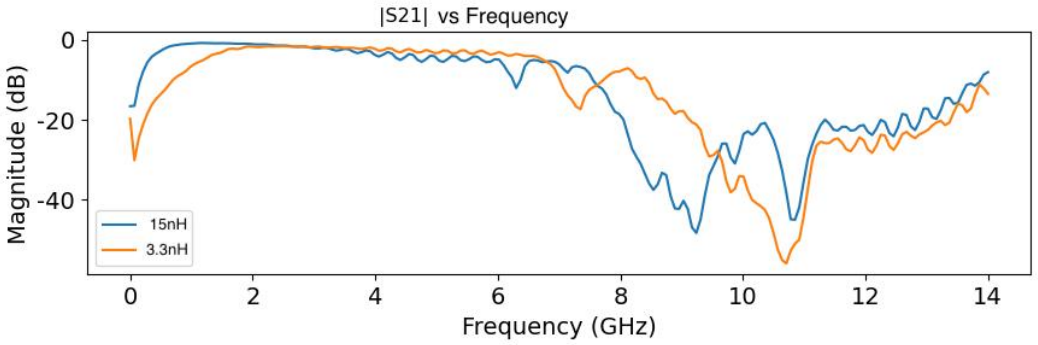

Figure 3.22.: Comparing S21 for the 3.3 nH PCB with the S21 for the 15 nH PCB. Neither PCB has wirebonds.

side of the ∼3.5 nH dip are very smooth. This opens up two good candidates for measurement bands, one between 1-3 GHz and another between 4-6 GHz. In summary, we came to the following conclusions: the 3.3 nH inductors led to the least insertion loss between 4-6 GHz, and the 33 nH inductors led to the least insertion loss around 1 GHz. The 15 nH inductors had almost as little insertion loss in both bands as either of those inductors, but also had the 'widest', or broadest frequency range, smooth spots between the resonance dip and the dip after 6 GHz. This made the 15 nH inductors the best choice to move forward with, as this PCB would be flexible for experimentation at both low (∼1 GHz) and high (∼4-6 GHz) frequencies.

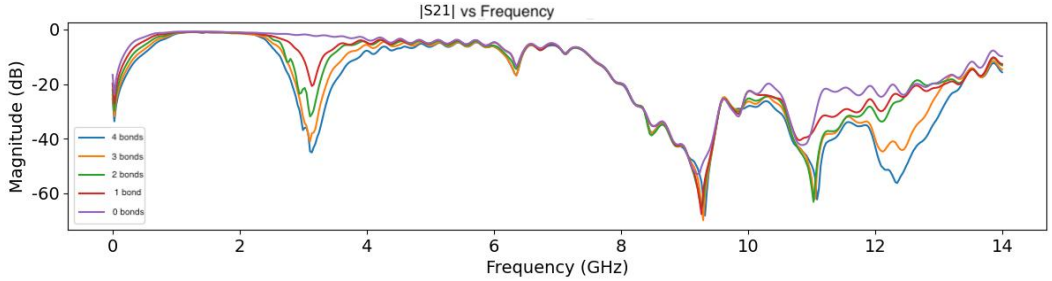

Figure 3.23.: Plucking off the wirebonds one by one and recording S21 vs frequency after each bond is plucked. Inductors are 15 nH.

There are broad ranges in which the transmission is adequate for reliably taking measurements with these PCBs. The creation of a PCB that moves bias tees off chip and on to the board at frequencies of several GHz is promising for future PCB designs, as previously on-board bias tees have been avoided aboce MHz frequencies. The next test will be to load them with a known sample in a dilution refrigerator. This requires the installation of a new microwave readout chain in the fridge.

4. Fridge Installation

This chapter documents the installation of the new readout chain into our dilution refrigerator 'Voyager'. Voyager is an Oxford Instruments Nanoscience Triton Cryofree dilution refrigerator capable of reaching temperatures below 20 mK, pictured here with the cans on in figure 4.1, and with the cans off in figure 4.2.

Figure 4.1.: Oxford Instruments dilution refrigerator 'Voyager'.

Figure 4.2.: Voyager opened up, without the cans on.

4.1. Measurement Circuit

The measurement circuit for our intended experiment is shown in figure 4.3. A signal will be sent from the VNA to the sample, either directly via a microwave coupler (for transmission measurements), or through a circulator which will allow reflection measurements to happen. The signal then passes through two circulators and an amplifier before entering either the input port of the VNA (for measurements of the S-parameters) or a spectrum analyzer for noise measurements. We needed to install the two circulators, the amplifier, and new superconducting cables leading to those components. It was also necessary to re-route one of the measurement lines to the circulator to enable reflection measurements. A higher frequency (4-8 GHz) microwave readout chain had already been installed in the fridge, but to access the frequencies needed in this experiment we needed new components.

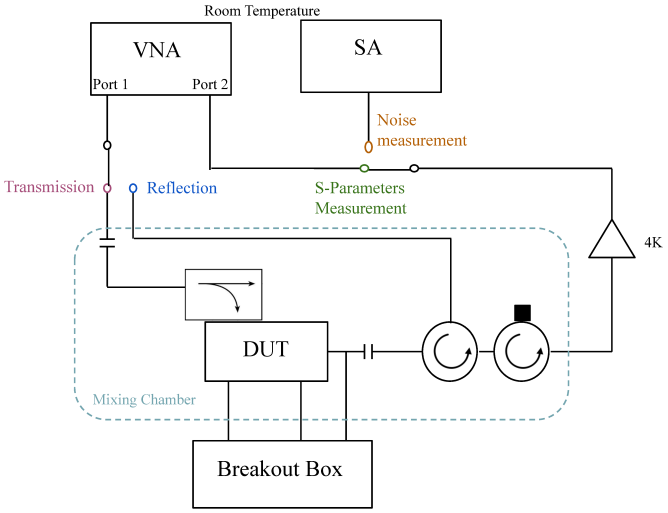

Figure 4.3.: Circuit representing the measurement chain of the experiment. VNA stands for Vector Network Analyzer, SA stands for Spectrum Analyzer, DUT stands for Device Under Test, the Breakout Box is the interface between measurement instruments and the DC lines at the sample, the colored circles represent different nodes of switches corresponding to transmission or reflection measurements, and S-parameter or noise measurements.

4.2. Low-Frequency Amplifier

The low frequency amplifier is the CITLF1 from Cosmic Microwave Technology, a SiGe low noise amplifier with an RF operating band from 0.001 to 1.5 GHz. It has a noise temperature of about 5 K and a gain of about 45 dB at 1 GHz. We chose this amplifier for the low-frequency microwave readout chain because it had a low noise temperature and high gain at 1 GHz. It was important that the amplifier's noise temperature wouldn't be so high as to obscure the noise signal that we wanted to measure, so we looked for amplifiers with the lowest noise temperatures that still had a reasonable gain and would then amplify the 'good' noise more than the 'bad' noise. The amplifier is installed on the 4 K plate because it operates best at slightly warmer temperatures than the mixing chamber. It is still installed in the cryostat rather than at room temperature so that the signal will be amplified before too much thermal noise gets added.

The amplifier cannot be directly bolted into the fridge, because the mounting holes provided on the amplifier are not the correct size to fit into the mounting holes on the fridge. We designed a small bracket similar to the one used for the other amplifier in the fridge, upon which the amplifier would be mounted. A suitable location was determined and the bracket was installed in the fridge. The bracket is made from copper, with gold plating on the outside. Then a small amount of low-temperature high-vacuum grease was applied to the bracket before screwing in the amplifier. The amplifier is pictured in figure 4.4. The amplifier is connected to line 8, as shown in section 2.3.2 figure 2.1.

The amplifier is powered by a separate power supply that sits outside the cryostat, while the

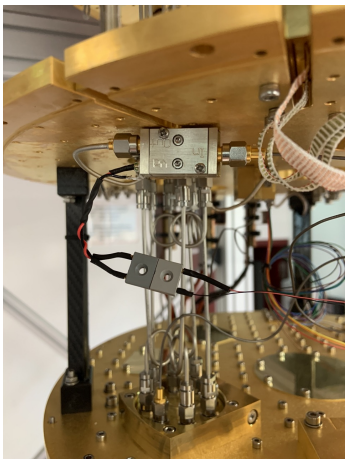

Figure 4.4.: Front view of the CITLF1 amplifier installed on the 4 K plate.

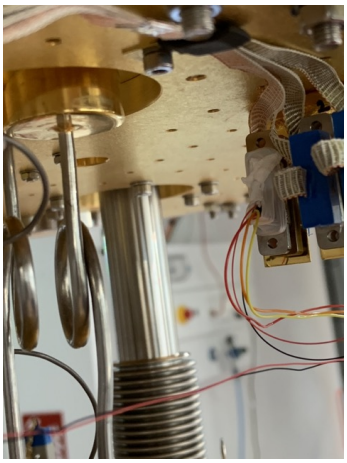

Figure 4.5.: Power supply wires are soldered to the connector.

amplifier itself sits on the 4 K plate of the cryostat. The power supply delivers power to the amplifier via cables that run from the top of the fridge down to the 4 K plate. These wires are soldered to two wires that then run to the amplifier and plug into the gray connector. The thin red and black wires shown in figure 4.5 power the low frequency amplifier and the other thicker wires belong to the other amplifier that was previously installed. The overall picture of the amplifier installation can be seen in figure 4.6 and figure 4.7. The bracket can be seen in figure 4.7, as the gold colored L-shaped bar behind the amplifier.

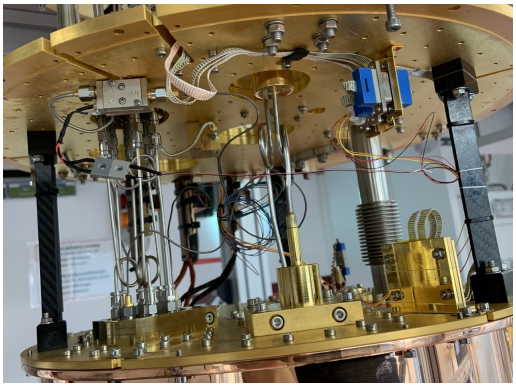

Figure 4.6.: The amplifier is powered by the thin red and black wires.

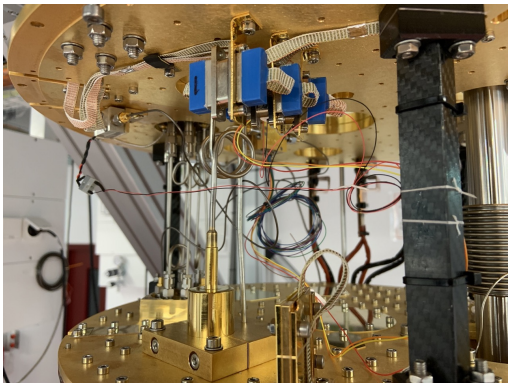

Figure 4.7.: Another angle of the amplifier installation.

It can be seen in figures 4.6 and 4.7 that the amplifier is connected on the input with a thin dark gray wire that comes from the bottom plate and makes a loop, and the output is connected to a copper coaxial cable (the shorter shiny silver wire). The thin dark gray wire is a superconducting wire, and is necessary for the thermalization reasons described in chapter two. The installation of the superconducting wires is described in section 4.4.

4.3. Circulators

The circulators were next to be installed. They are the 1.35-1.75 GHz cryogenic circulators from Raditek. These circulators were chosen because they are the only available circulators that operate near 1 GHz. Each circulator is approximately 5 cm by 5.5 cm by 4 cm. The installation circuit is shown in figure 4.8.

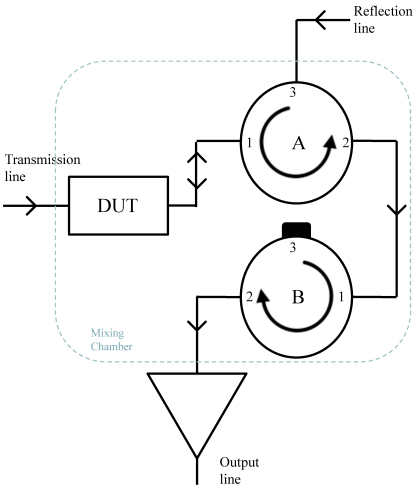

Figure 4.8.: Installation circuit of the circulators.

The circulators were installed on the mixing chamber plate because it is important that they operate at the same temperature as the sample. RF components can add a lot of unwanted noise to a signal, so it is best that they are placed as close as possible to the device and at the same temperature to try to limit the noise generated. However, there was not enough space to place the two circulators side by side. Instead we installed one circulator on the top of the plate and one underneath the plate. For the purposes of the circuit diagram, the circulator underneath the plate is referred to as circulator 'A' and the one on top is circulator 'B'. Due to this, the circulators are mirrored with respect to one another. In figure 4.9 and figure 4.10, the locations of the two circulators are shown.

Similarly to the amplifier, we also needed to design a bracket to hold the circulators to the mixing chamber plate. This too is in an L-shape, and is copper plated with gold. Because the circulators are heavy and large, it needed to be a large bracket with many screw holes to reduce the torque on the fridge. A view of how the circulators are bolted to the fridge is seen in figure 4.11. Unlike with the amplifier, the mixing chamber is so cold that adding grease in between the circulator and the bracket or the bracket and the mixing chamber will not help thermalize the circulators.

The output port of circulator 'B' was connected to line 8, where it will be connected to the amplifier via superconducting coaxial cables. The reflection port (port 3 of circulator 'A') was connected to by a coaxial cable from line 7. This means that line 7 would no longer

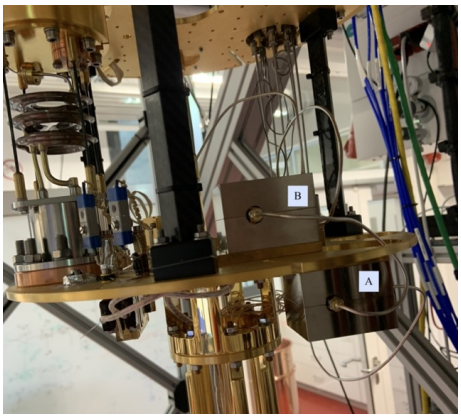

Figure 4.9.: A side view of the installed circulators

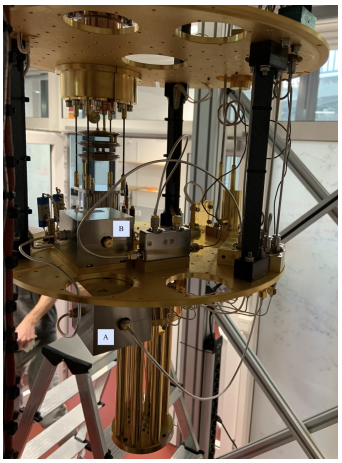

Figure 4.10.: A front view of the installed circulators

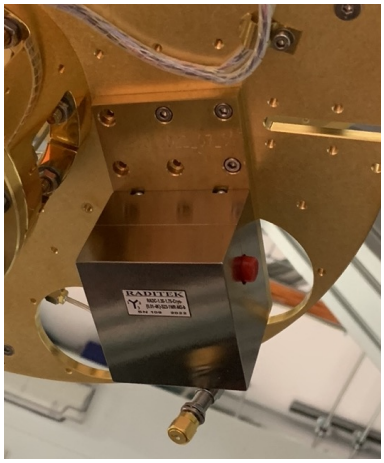

Figure 4.11.: Demonstration of how the circulators are bolted to the mixing chamber.

run down to the sample directly, and can only reach the sample through the circulator. The full diagram of the microwave wiring is included in section 2.3.2, figure 2.1. The last piece of installation that was required was the building and installing of superconducting coaxial cables. These cables are needed due to thermalization of the signal as it travels up the fridge.

4.4. Superconducting Coaxial Cables

Superconducting coaxial cables can greatly increase the quality of the experiment because they carry the current without adding any resistance, therefore without adding any extra noise. They are also expensive, difficult to prepare, and easy to break. The process of preparing the cables is described in the coming section.

4.4.1. Preparation

The coaxial cable is made from a center conductor of niobium titanium (NbTi) that is insulated by a layer of Polytetrafluoroethylene (PTFE, Teflon brand name). The cable is

encased in niobium. The coaxial cable arrived from the company *Intelliconnect* as one long straight wire, and we cut and formed it into the required shape. We measured the distances between plates of the cryostat, and then added another couple centimeters to allow for making loops and 'S' shapes in the wire, and then added a couple of centimeters to allow for mistakes. The loops and 'S' shapes are necessary, because when the fridge cools down, the thermal expansion of the wire changes and if there are no coils to allow for stretching and shrinking then the wire could break.

After the sections of wire are cut to the correct lengths, the center conductor on either end is filed down to a sharp point, in order to attach the connectors. As the center conductor is very sensitive it requires care not to accidentally nick it while cutting away the outer conductor and the PTFE. The general procedure is to lightly cut a circle around the outer conductor about 3 mm away from the edge, without pressing deep enough to cut into the center conductor. The PTFE also needs to either be cut away or stuffed backwards into the niobium casing. Then once 3 mm of center conductor are exposed, it is filed to a sharp point with a filing board. A picture demonstrating the preparation of a cable up to this step is included in figure 4.12.

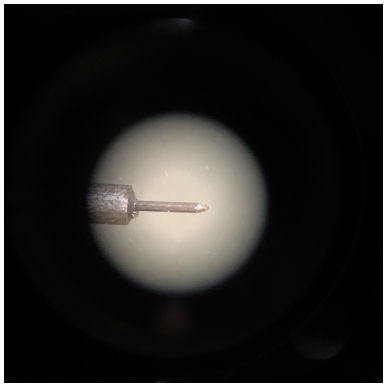

Figure 4.12.: The tip of the superconducting coaxial cable before it is crimped into the connector.

After all the ends of the coaxes are sharpened, the connectors can be attached to the ends. The *Intelliconnect* coaxial cable system uses SMA crimp-connectors, which crimp onto the ends of the coaxial cable by force. To ensure that the connection is good, that the ends of the coaxial cables need to go straight into the ends of the SMA connectors. In figure 4.14, a correctly connected cable is shown.

In the next step, the cables are shaped. The material is rigid, but can be bent slowly without breaking. The round barrel of a torque wrench can be used as the bending fulcrum. Applying small amounts of pressure as the cable is pressed against the wrench, it is possible to form a loop into each cable. For the cable that attached the input of the amplifier with the still plate, a further 'S' shape had to be bent, such that the cable could connect at an angle with the amplifier. An example of a bent coaxial cable is shown in figure 4.15 and figure 4.13.

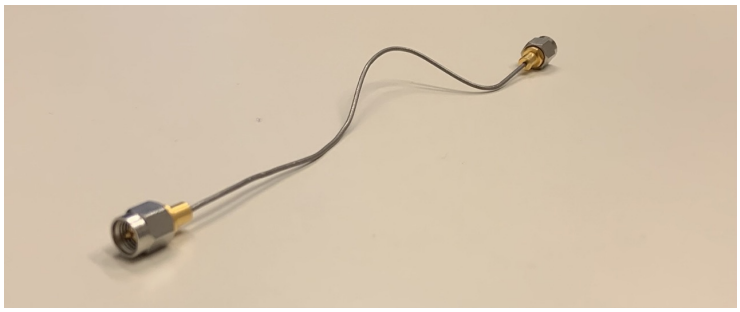

Figure 4.13.: The superconducting coaxial cable with 'S' shapes formed.

Each cable had to be bent to fit the stage at which it would be used, and to accommodate plugging into different components at their locations.

Figure 4.14.: A superconducting coaxial cable inserted into the SMA crimp connector.

Figure 4.15.: The superconducting coaxial cable with 'S' shapes formed.

Lastly, the coaxial cables are installed into the fridge. This is a delicate process, as the column which holds the cables requires a bit of force to maneuver, and if the column moves rapidly it could break not only the superconducting coaxial cables but also the regular stainless steel coaxial cables.

4.4.2. Installation

From the bottom of the fridge up, the first cable was installed between the mixing chamber and the cold plate. The output port of circulator 'B' is attached to the bottom of the mixing chamber plate with a copper coaxial cable, and then from there a superconducting coaxial cable leads from the mixing chamber stage to the cold plate, see figure 4.16. From the cold plate to the still plate there is another superconducting coaxial cable, shown in figure 4.17. And lastly there is one more superconducting coaxial cable connected from the bottom of the still plate to the input of the amplifier on the 4 K plate, which can be seen in figure 4.6.
The coaxial cables were then tested to ensure that the transmission through each was without

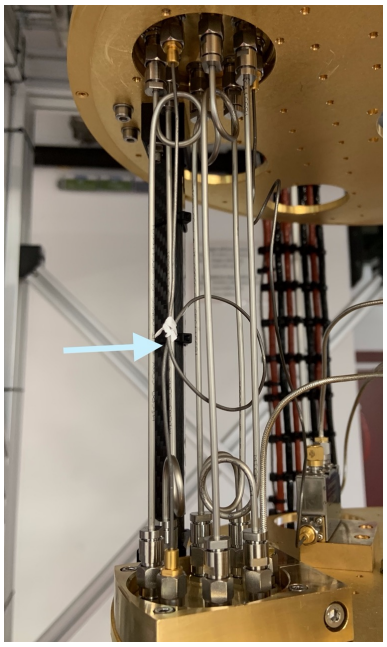

Figure 4.16.: Superconducting coaxial cable installed between the mixing chamber and the cold plate.

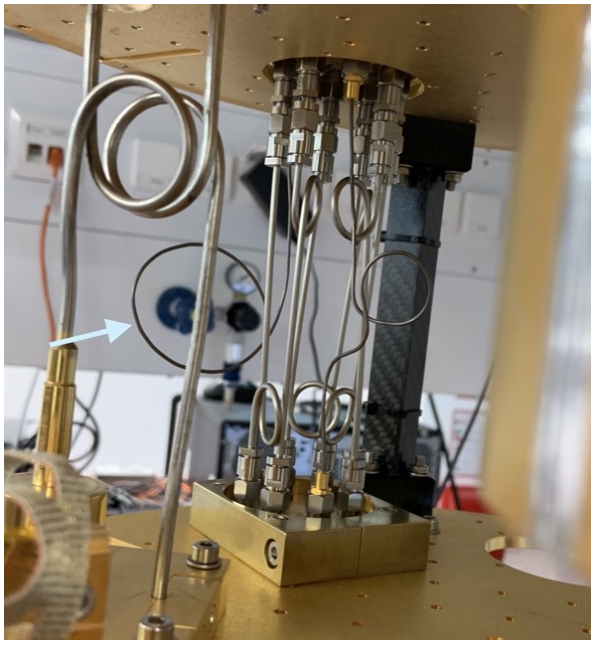

Figure 4.17.: Superconducting coaxial cable installed between the still plate and the cold plate.

resonances and with very little insertion loss. Over the frequency range of interest (∼1 GHz), there was typically less than 3 dB of loss for each cable. Additional figures for the testing of each cable are included in the appendix E.

4.5. Calibration

After installation, we checked that all the components behave as expected. The superconducting coaxial cables have already been individually checked (see appendix E), but that leaves the rest of the measurement chain to test. The easiest way to do this is to check first the transmission setup in an S21 configuration with the VNA, and then test the reflection setup.

As a first check, the amplifier is tested aside from the rest of the setup, by unplugging the input port of the amplifier, and connecting it directly to the VNA output port 1. Then, the output of the amplifier through the cryostat is connected to the input port of the VNA (port 2). The resulting S21 magnitude is the gain profile of the amplifier, and is shown in figure 4.18. The overall profile makes sense when compared against the gain vs frequency figure shown in the data sheet.

With the knowledge that the amplifier is working as expected, we moved on to testing the remainder of the circuit. A cable is connected directly from the output of the VNA to the bottom of the fridge, on line 8 (the output line of my circuit) and the input of the VNA is connected to line 8 from the top of the fridge. We measure the S21 magnitude of the entire

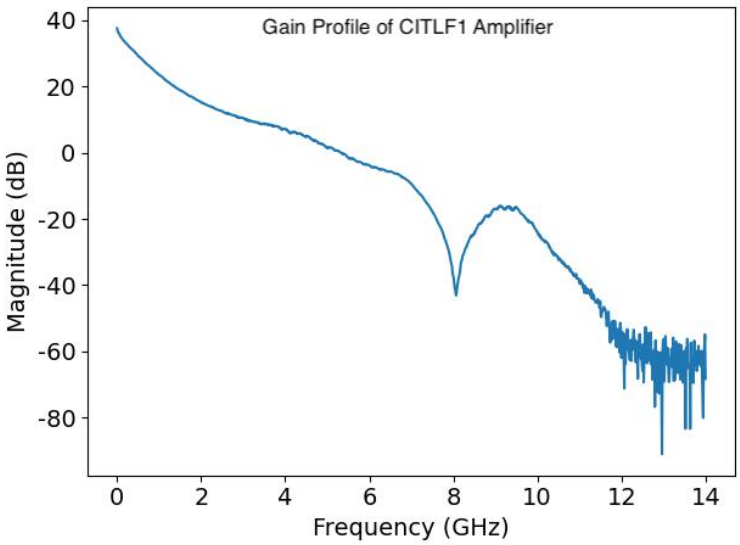

Figure 4.18.: Gain profile of the newly installed amplifier.

line (the green trace in figure 4.19). The VNA power in this case was -30 dBm, and the gain of the amplifier should be about 42 dB around 1.5 GHz. If we look more closely around 1 GHz it becomes easier to see that the S21 magnitude in the transmission setup is about 18 dB, see figure 4.20. This means that there is an insertion loss of about 3 dB due to the cables which is entirely reasonable. An insertion loss of about 3 dB should not have a particularly adverse effect on the experiment. Additionally, we expect that the performance gets better at lower temperatures, as the components are meant to be used at low temperatures. Additionally, the circulators' bandwidth is specified to be 1.35-1.75 GHz where we can assume a small amount of 'overflow' band on either side of that. This can explain why between 0-1.2 GHz there is some unwanted behavior, namely resonances and more noise, and why the signal drops off abruptly near 1.8 GHz.

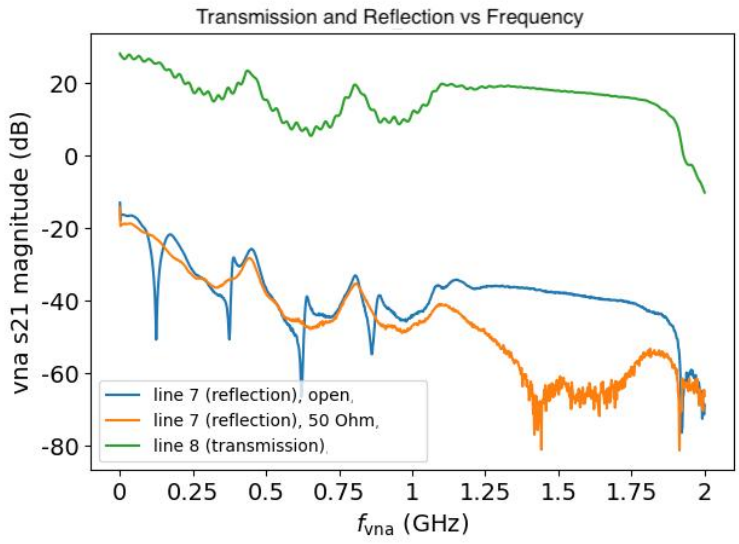

Figure 4.19.: Checking the installation path.

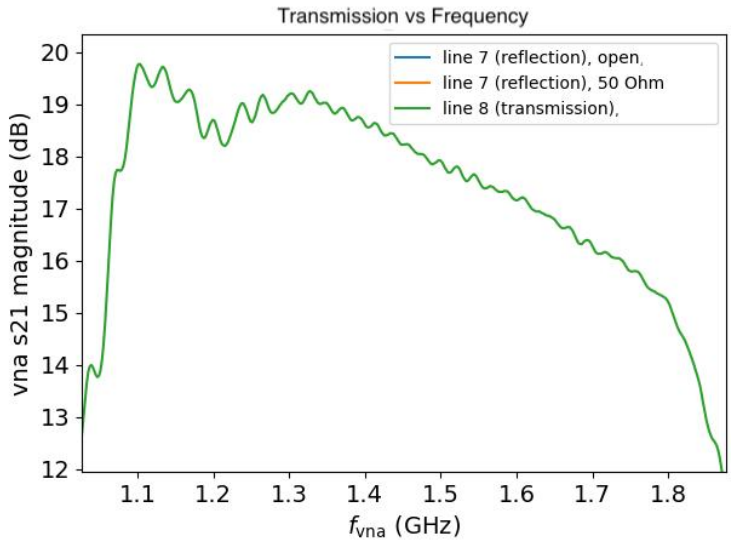

Figure 4.20.: Zoom in to 1 GHz on the transmission setup S21 trace.

Next we tested the reflection setup. The VNA output port was connected to line 7 (the reflection line). The signal then passes through the top of the fridge, through 50 dB of attenuation, through one circulator, and then down to the open port at the bottom of the fridge. The input port of the VNA was connected to line 8 (the output of the measurement line). This setup measures the reflection off the open circuit. We expect this test to have a very similar shape as the transmission test, but at lower S21 magnitude because of the added attenuation on line 7. This expectation was met, as shown in figure 4.19, as the blue line shows lower S21 magnitude than for the transmission setup. We also tested closing the open port with a 50 Ω cap, to check that the S21 magnitude dropped even further (as most of the signal would be dumped into the cap). This was also demonstrated in figure 4.19. In figure 4.21, we see that the S21 magnitude around 1.5 GHz is -38 dB. In comparison with the transmission setup magnitude around 1.5 GHz of 18 dB, there is a difference of about 56 dB. This is attributed to the 50 dB attenuation on the reflection setup's line from the top of the fridge down to the open port, plus a few dB due to losses in the cables (3 dB on the way down, and 3 dB on the way back up).

Now that the components have been tested, the next step is the calibration of the experiment. It was decided to create a calibration device - a device whose behavior we can predict with relative certainty. This way, we will know if the entire measurement chain is working as anticipated, and we will be able to compare later results with the anomalous metal sample to the results of this 'test' chip.

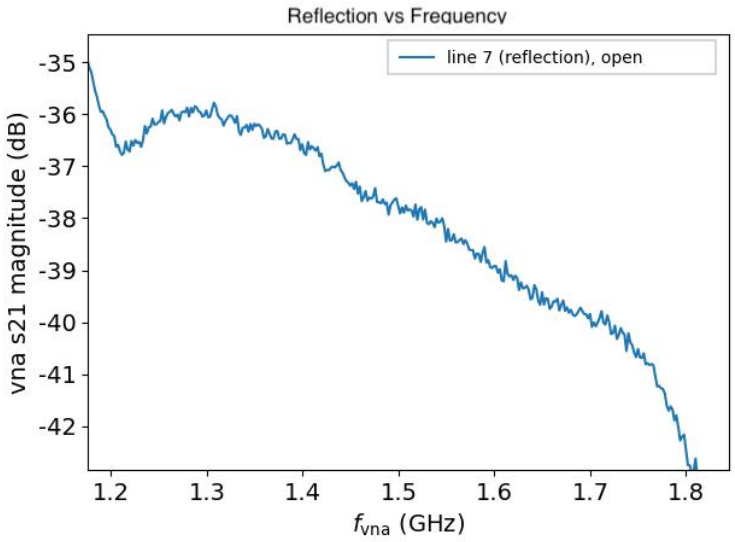

Figure 4.21.: Zoom in to 1 GHz on the reflection setup S21 trace.

5. Sample Preparation and Measurement

The calibration sample was decided to be a simple aluminum transmission line. A superconducting transmission line should behave like a normal superconducting wire, whose behavior is well understood. By loading an aluminum transmission line fabricated on a chip, we will be able to test every part of the setup, from the PCB to the newly installed components in the fridge, to the room temperature measurement setup. And the results from the calibration device will prove useful when it comes time to test the 'real' device.

The calibration device was designed to be as close to the final experimental device as possible. This means that two voltage probes were also included, because eventually we would like to measure four-probe resistance. Two additional smaller devices were fabricated on the same chip as well, to test transport properties of the devices. The device layout and fabrication was completed in collaboration with PhD student Duc Phan. We used CAD software to design the chip, which was read by the electron beam lithography machine and fabricated according to the procedures outlined in the above chapter on nanofabrication. We then loaded the chip to the fridge.

5.1. Calibration Device

The device is named 'h2', and can be seen in figure 5.1. It was wirebonded to the PCB, to connect the device to the microwave transmission and to connect the two voltage probes to DC pads at the bottom of the chip, as well as connecting the ground plane of the chip to the ground plane of the PCB. Then we loaded the PCB and chip into the puck, see figure 5.3 and figure 5.2. The SMP connectors on the left and right side of the PCB are connected to with the gray cables seen in figure 5.3, and the DC connections are made by the large edgecard connector on the top of the filter PCB, that has many colorful wires coming out of it. The left SMP connector is connected to one of the free lines in the cryostat (lines 1-3), while the right SMP connector is connected to line 8, the newly installed output line.

The puck was then loaded into the fridge, and cooled down. We first took a trace of the chip in the transmission setup, where we sent a signal to the left SMP connector, and measure the output from the right side. We compared the results from this measurement to a throughline test of the amplifier, shown in figure 5.4. The trace of the h2 device has some resonances, but within the band of the amplifier and circulators is relatively smooth. The throughline test was completed on another cooldown by loading a wire from a free line (lines 1-3) to line 8 and then measuring the S21 magnitude. There is a short section where the difference in

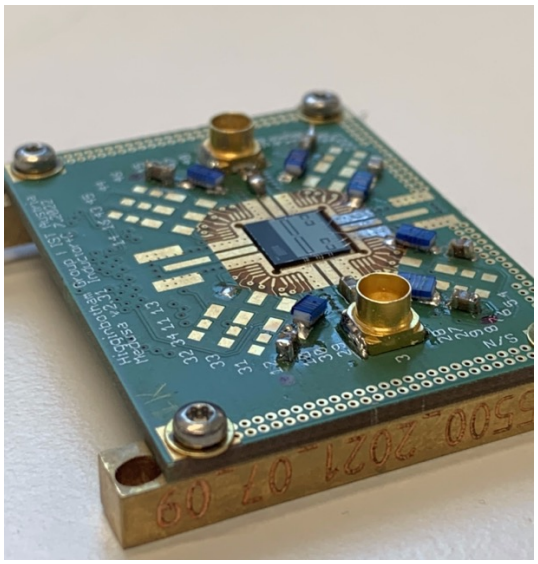

Figure 5.1.: The h2 calibration device set up in the PCB.

Figure 5.2.: A close up view of the h2 device.

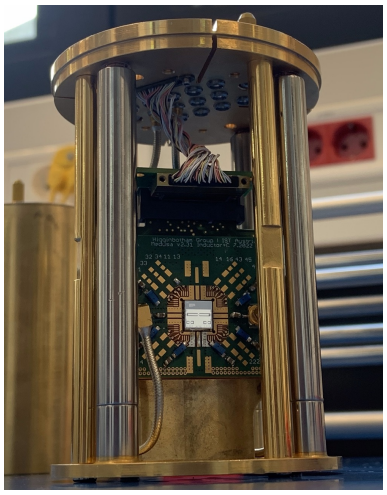

Figure 5.3.: The h2 device loaded into the puck.

magnitude between the h2 chip and the amplifier alone is nearly zero, signifying this region as potentially a good region for measurements. This would be a good region for measurements because it is in the band of the circulators and amplifier, and the h2 chip seems to show nearly no additional loss. Additionally, this region occurs right at the frequency of interest, 1 GHz.

We then also removed the chip from the fridge and re-loaded it on the old (higher frequency) measurement chain, to get an idea of how the transmission spectrum looked on a known measurement chain. This measurement readout chain is meant to operate between 4-8 GHz, and so would also check how well the PCB and chip work at higher frequencies as was the back-up plan. The results of this measurement are shown in figure 5.5. Once again we ran a throughline in order to test the amplifier with just a wire as the test 'device'. As can be

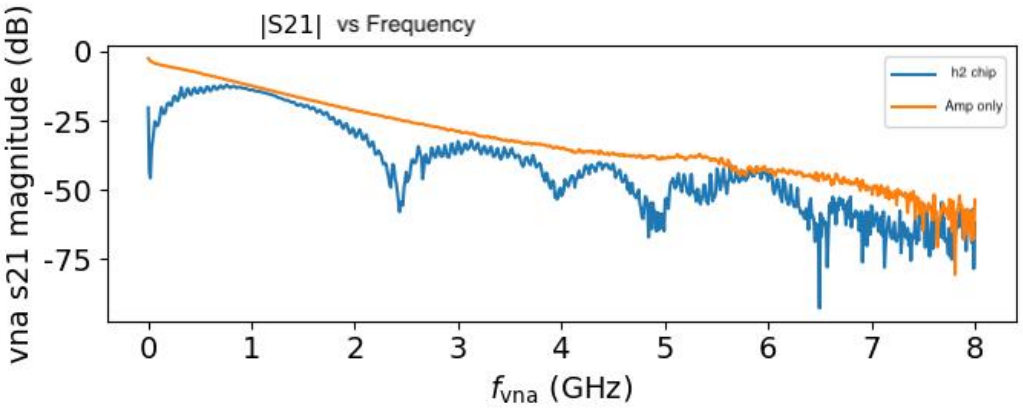

Figure 5.4.: Comparing the transmission setup S21 magnitude of the h2 chip to the transmission setup S21 magnitude of the amplifier alone.

seen, there are more resonances in the higher frequency region than there were in the lower frequency region. But there is yet again a small band near 6 GHz in which the S21 magnitude of the h2 chip is not much less than that of the amplifier with a throughline, which may prove a good region for experimentation at higher frequency.

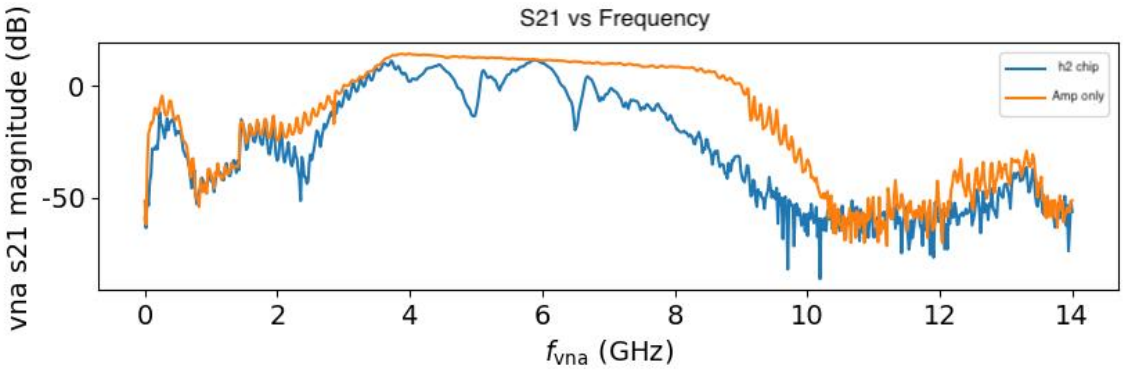

Figure 5.5.: Comparing the transmission of h2 in the higher frequency measurement chain.

Overall the results from the first round of calibration device testing are promising. The transmission spectrum of the device shows regions where we could potentially measure the real device. Due to time constraints and demand for use of the fridge, further experimentation of the calibration device is put on hold. In the meantime, we begin planning the real device.

5.2. Experimental Device

Now it is finally time to create the anomalous metal device. We designed the layout of the device in CAD and fabricated the device. The device is a two-dimensional Josephson junction array on top of a semiconductor heterostructure, where a two-dimensional electron gas (2DEG) is created in the quantum well formed in the layers of the semiconductor. The

superconductivity of the aluminum Josephson junction array is coupled to the 2DEG which provides a platform where the carrier density can be tuned by use of a gate. The design of this device is modeled after the devices fabricated by Bøttcher et. al. in [29] and [45]. The array is 40 by 100 $1\,\mu m^2$ junctions. There is a separation distance of $0.15\,\mu m$ between superconducting islands, so each unit cell is $1.15\,\mu m^2$. The dielectric between the aluminum islands and the top gate is 40 nm of Al_2O_3, and the top gate is made of aluminum. There are two voltage probes leading to the device to use in measuring the four-probe resistance. On the chip, there are four total devices: the main device is in the center, where microwave signal as well as a DC bias can be applied across the device, and then two smaller devices on the bottom left and right of the device which are copies of the main device (the arrays have the same dimensions as the main device), and the final device in the upper right corner is another aluminum transmission line just like the h2 calibration device.

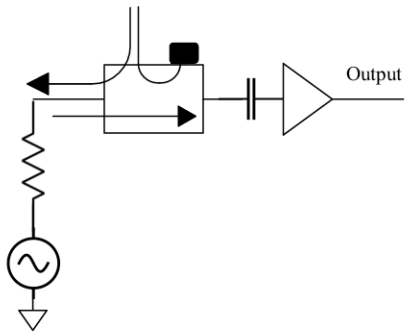

Figure 5.6.: Schematic showing how the microwave signal (the arrow) is coupled to the device (modeled here as a resistor), and where the noise comes from (modeled as a voltage source).

One major difference to the h2 calibration chip, however, is that the microwave signal is now coupled to the device instead of being sent straight in. The noise that we want to measure comes from the resistance of the device, and can be modeled as a resistor which has a small voltage source connected to ground. This means that one side of the device needs to be grounded in order to generate the right kind of noise, and therefore the microwave signal needs to be coupled in to the circuit rather than being sent directly across the sample as in the h2 device configuration. A schematic of the setup is shown in figure 5.6. We performed several simulations of a microwave coupler to this device to determine the right dimensions to get maximum coupling at the right impedance. The main results of these simulations are presented in appendix F.

With the microwave coupling design decided, the chip was fabricated and prepared for measurement. The PCB was placed over the sample holder and the chip was adhered to the sample holder with silver paste, see figure 5.7. The sample is named 'h3'. Each of the four devices on the chip are visible, the main device in the middle with the microwave coupler, the two smaller devices on the bottom, and the aluminum transmission line device in the upper right corner. As can be seen in figure 5.7, all the bias tee lines are in use for this chip. A close up of the wirebonding is shown in figure 5.8.

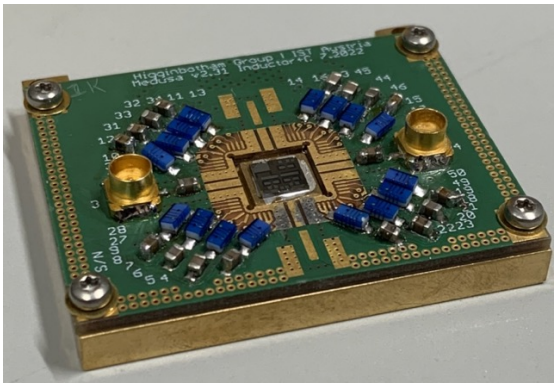

Figure 5.7.: Sample h3 in the PCB and sample holder before wirebonding.

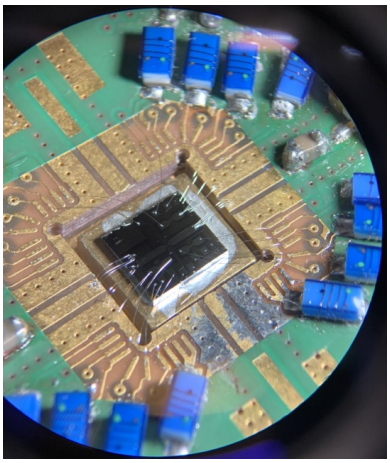

Figure 5.8.: Close up view of the wirebonds on the h3 chip, through a microscope.

We then attached the filter PCB, loaded the wirebonded chip in to the puck, and attached the SMP connectors and the edge card connector, as seen in figure 5.9 and figure 5.10. Making sure to note the orientation of the sample within the puck (so that we know which direction will be perpendicular or parallel to the magnetic field once the sample has been loaded), the puck and sample are then loaded together in to the fridge. We then checked that every wirebonded line was properly connected.

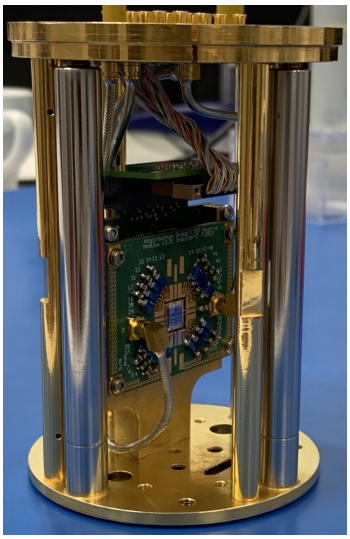

Figure 5.9.: The h3 chip ready to be loaded into the cryostat.

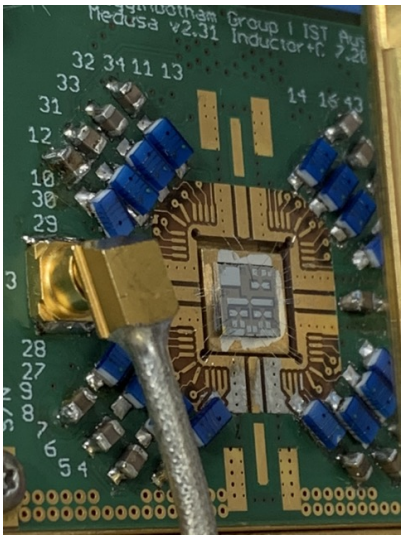

Figure 5.10.: Close up view of the h3 chip in the puck.

The first measurement we did with this device was to take an IV curve. This measurement is shown in figure 5.11. The device shows a supercurrent feature between roughly -20 and 20 μV, indicating a superconducting regime that at some critical voltage (or current) the sample becomes resistive (normal).

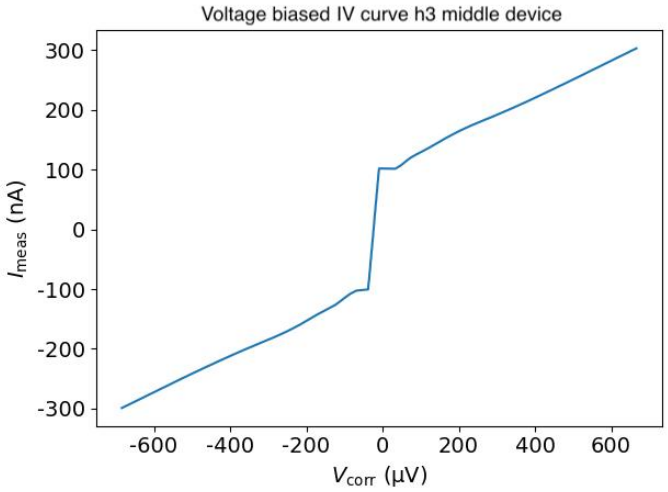

Figure 5.11.: Biasing voltage and measuring current of the h3 middle device at zero gate voltage and zero magnetic field.

We then wanted to test that the gate was working so we swept the gate voltage from 0 to -5 V and measured the resulting current. It is shown in figure 5.12 that the device maintains a constant current (meaning a zero-resistivity and superconducting state) until a certain voltage is reached (around -3.9 V), at which point the resistance of the device starts to increase rapidly with increasing voltage. Eventually the measured current seems to reach zero nA, suggesting that the system is beginning to enter an insulating phase. However there is a span of about 1 V over which the resistance (calculated from the slope of the measured current) is finite, suggesting that it could be in the anomalous metal phase. This demonstrates that the gate is working and the device has a strong dependence on the gate voltage. To then measure the noise of this system it will be possible to change the output of the measurement chain from VNA port 2, to the spectrum analyzer. Then we can measure the noise power of the device. Further images of the measurement setup at room temperature are shown in appendix G.

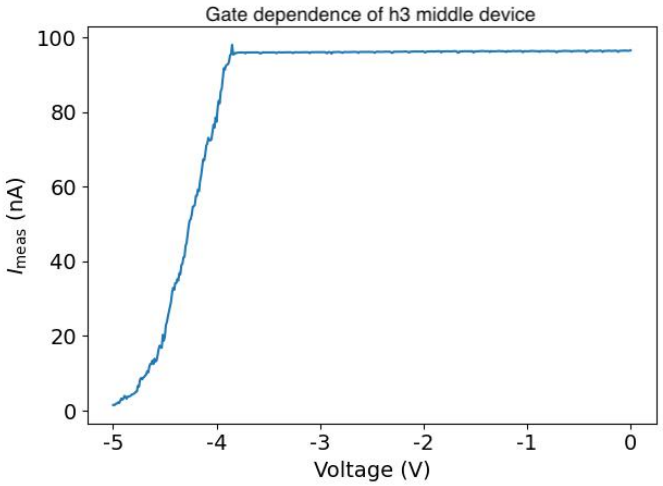

Figure 5.12.: Gate dependence of the resistivity of the middle device on the h3 chip.

With these two measurements, we have demonstrated that the device superconducts and has a superconducting critical current. The device is also gate-dependent. This is sufficient evidence that further measurements into the anomalous metal phase and eventually the noise characterization of this phase are warranted with this device. Thus, the goal of this thesis project has been reached: to design an experiment in which to test the anomalous metal phase's noise dependence.

6. Conclusions and Outlook

This experiment has led to the development of a platform for characterizing electric noise in the anomalous metal phase. This is a progression that promises to bring clarity to the field, and help to further explain the anomalous metal phenomenon. The results of this thesis also have implications beyond just this project: the PCBs with on-board bias tees developed are now used by many members of our group. Additionally, the successful installation of several new components to the fridge provided a new measurement readout chain to probe at lower frequencies. Tests of the first calibration device proved that we have been successful in preparing an experiment to measure the anomalous metal phase. Lastly, the final experimental device showed promise on the first round of experimentation in the fridge.

The outlook for the future of this experiment is promising. Measurements will be taken in the coming months that will help to solidify the first results shown in this thesis. The observation of noise signatures that confirm that proper thermalization is occurring (meaning that the sample is not heating up) in the anomalous metal phase would be a major result - providing evidence that the phase is 'real' and not due to experimental oversight. Furthermore, observation of a difference in the behavior of the noise between the superconducting, insulating, and anomalous metal phases could provide further evidence as to the distinction of the anomalous metal phase. The noise in this phase has been predicted to obey a universal scaling form as proposed by Green et. al.[35] that links noise of this form to the quantum version of the fluctuation-dissipation theorem[50]. The experiment prepared in this thesis could empirically confirm this connection.

Bibliography

[1] F. London, H. London, and Frederick Alexander Lindemann. The electromagnetic equations of the supraconductor. *Proceedings of the Royal Society of London. Series A - Mathematical and Physical Sciences*, 149(866):71–88, 1935.

[2] Charles Kittel. *Introduction to solid state physics*. Wiley, Hoboken, NJ, 8th ed edition, 2005.

[3] Lev Davidovich Landau and Dirk Ter-Haar. *Collected papers of L.D. Landau*. Pergamon, Oxford, 1965.

[4] Tinkham Michael. *Introduction to Superconductivity*. Dover Publications, 2004.

[5] Leon N. Cooper. Bound electron pairs in a degenerate fermi gas. *Phys. Rev.*, 104:1189–1190, Nov 1956.

[6] J. Bardeen, L. N. Cooper, and J. R. Schrieffer. Microscopic theory of superconductivity. *Phys. Rev.*, 106:162–164, Apr 1957.

[7] J. Bardeen, L. N. Cooper, and J. R. Schrieffer. Theory of superconductivity. *Phys. Rev.*, 108:1175–1204, Dec 1957.

[8] M. K. Wu, J. R. Ashburn, C. J. Torng, P. H. Hor, R. L. Meng, L. Gao, Z. J. Huang, Y. Q. Wang, and C. W. Chu. Superconductivity at 93 k in a new mixed-phase y-ba-cu-o compound system at ambient pressure. *Phys. Rev. Lett.*, 58:908–910, Mar 1987.

[9] J. G. Bednorz and K. A. Muller. Possible high Tc superconductivity in the Ba-La-Cu-O system. *Z. Phys. B*, 64:189–193, 1986.

[10] A. Schilling, M. Cantoni, J. D. Guo, and H. R. Ott. Superconductivity above 130 k in the hg–ba–ca–cu–o system. *Nature*, 363(6424):56–58, May 1993.

[11] Jan Zaanen, Yan Liu, Ya-Wen Sun, and Koenraad Schalm. *Holographic Duality in Condensed Matter Physics*. Cambridge University Press, 2015.

[12] A. Schilling, M. Cantoni, J. D. Guo, and H. R. Ott. Superconductivity above 130 k in the hg–ba–ca–cu–o system. *Nature*, 363(6424):56–58, May 1993.

[13] Hiroki Takahashi, Kazumi Igawa, Kazunobu Arii, Yoichi Kamihara, Masahiro Hirano, and Hideo Hosono. Superconductivity at 43 k in an iron-based layered compound lao1-xfxfeas. *Nature*, 453(7193):376–378, May 2008.

[14] Yuan Cao, Valla Fatemi, Ahmet Demir, Shiang Fang, Spencer L. Tomarken, Jason Y. Luo, Javier D. Sanchez-Yamagishi, Kenji Watanabe, Takashi Taniguchi, Efthimios Kaxiras, Ray C. Ashoori, and Pablo Jarillo-Herrero. Correlated insulator behaviour at half-filling in magic-angle graphene superlattices. *Nature*, 556(7699):80–84, April 2018.

[15] H. M. Jaeger, D. B. Haviland, B. G. Orr, and A. M. Goldman. Onset of superconductivity in ultrathin granular metal films. *Phys. Rev. B*, 40:182–196, Jul 1989.

[16] Thomas Vojta. Quantum phase transitions in electronic systems. *Annalen der Physik*, 512(6):403–440, June 2000. arXiv:cond-mat/9910514.

[17] Bertrand Berche, Tim Ellis, Yurij Holovatch, and Ralph Kenna. Phase transitions above the upper critical dimension. *SciPost Phys. Lect. Notes*, page 60, 2022.

[18] Yen-Hsiang Lin, J. Nelson, and A.M. Goldman. Superconductivity of very thin films: The superconductor–insulator transition. *Physica C: Superconductivity and its Applications*, 514:130–141, July 2015.

[19] J M Kosterlitz and D J Thouless. Ordering, metastability and phase transitions in two-dimensional systems. *Journal of Physics C: Solid State Physics*, 6(7):1181, apr 1973.

[20] D. B. Haviland, Y. Liu, and A. M. Goldman. Onset of superconductivity in the two-dimensional limit. *Phys. Rev. Lett.*, 62:2180–2183, May 1989.

[21] Aharon Kapitulnik, Steven A. Kivelson, and Boris Spivak. *Colloquium* : Anomalous metals: Failed superconductors. *Reviews of Modern Physics*, 91(1):011002, January 2019.

[22] Steven Weinberg. From bcs to the lhc, January 2008. [Online; accessed 06-Feb-2023].

[23] N. D. Mermin and H. Wagner. Absence of ferromagnetism or antiferromagnetism in one- or two-dimensional isotropic heisenberg models. *Phys. Rev. Lett.*, 17:1133–1136, Nov 1966.

[24] P. C. Hohenberg. Existence of long-range order in one and two dimensions. *Phys. Rev.*, 158:383–386, Jun 1967.

[25] E. Abrahams, P. W. Anderson, D. C. Licciardello, and T. V. Ramakrishnan. Scaling theory of localization: Absence of quantum diffusion in two dimensions. *Phys. Rev. Lett.*, 42:673–676, Mar 1979.

[26] S. Das Sarma and E.H. Hwang. The so-called two dimensional metal–insulator transition. *Solid State Communications*, 135(9):579–590, 2005. Fundamental Optical and Quantum Effects in Condensed Matter.

[27] Bertrand I. Halperin. On the hohenberg–mermin–wagner theorem and its limitations. *Journal of Statistical Physics*, 175(3):521–529, May 2019.

[28] N. Mason and A. Kapitulnik. Dissipation effects on the superconductor-insulator transition in 2d superconductors. *Phys. Rev. Lett.*, 82:5341–5344, Jun 1999.

[29] C. G. L. Bøttcher, F. Nichele, M. Kjaergaard, H. J. Suominen, J. Shabani, C. J. Palmstrøm, and C. M. Marcus. Superconducting, insulating and anomalous metallic regimes in a gated two-dimensional semiconductor–superconductor array. *Nature Physics*, 14(11):1138–1144, November 2018.

[30] Ebrahim Sajadi, Tauno Palomaki, Zaiyao Fei, Wenjin Zhao, Philip Bement, Christian Olsen, Silvia Luescher, Xiaodong Xu, Joshua A. Folk, and David H. Cobden. Gate-induced superconductivity in a monolayer topological insulator. *Science*, 362(6417):922–925, 2018.

[31] A. D. Rata, V. Kataev, D. Khomskii, and T. Hibma. Giant positive magnetoresistance in metallic vo_x thin films. *Phys. Rev. B*, 68:220403, Dec 2003.

[32] Nicholas P. Breznay and Aharon Kapitulnik. Particle-hole symmetry reveals failed superconductivity in the metallic phase of two-dimensional superconducting films. *Science Advances*, 3(9):e1700612, 2017.

[33] Wei Liu, LiDong Pan, Jiajia Wen, Minsoo Kim, G. Sambandamurthy, and N. P. Armitage. Microwave spectroscopy evidence of superconducting pairing in the magnetic-field-induced metallic state of ino_x films at zero temperature. *Phys. Rev. Lett.*, 111:067003, Aug 2013.

[34] Youcheng Wang, I. Tamir, D. Shahar, and N. P. Armitage. Absence of cyclotron resonance in the anomalous metallic phase in ino_x. *Phys. Rev. Lett.*, 120:167002, Apr 2018.

[35] A. G. Green, J. E. Moore, S. L. Sondhi, and A. Vishwanath. Current Noise in the Vicinity of the 2D Superconductor-Insulator Quantum Critical Point. *Physical Review Letters*, 97(22):227003, December 2006.

[36] Julian Sonner and A. G. Green. Hawking Radiation and Nonequilibrium Quantum Critical Current Noise. *Physical Review Letters*, 109(9):091601, August 2012.

[37] R. C. Jaklevic, John Lambe, A. H. Silver, and J. E. Mercereau. Quantum interference effects in josephson tunneling. *Phys. Rev. Lett.*, 12:159–160, Feb 1964.

[38] T. A. Fulton, P. L. Gammel, D. J. Bishop, L. N. Dunkleberger, and G. J. Dolan. Observation of combined josephson and charging effects in small tunnel junction circuits. *Phys. Rev. Lett.*, 63:1307–1310, Sep 1989.

[39] V Bouchiat, D Vion, P Joyez, D Esteve, and M H Devoret. Quantum coherence with a single cooper pair. *Physica Scripta*, 1998(T76):165, jan 1998.

[40] Piero Martinoli and Chris Leemann. Two dimensional josephson junction arrays. *Journal of Low Temperature Physics*, 118(5):699–731, Mar 2000.

[41] P. W. Anderson and A. H. Dayem. Radio-frequency effects in superconducting thin film bridges. *Phys. Rev. Lett.*, 13:195–197, Aug 1964.

[42] Ch. Leemann, Ph. Lerch, G. A. Racine, and P. Martinoli. Vortex dynamics and phase transitions in a two-dimensional array of josephson junctions. *Phys. Rev. Lett.*, 56:1291–1294, Mar 1986.

[43] H. S. J. van der Zant, F. C. Fritschy, W. J. Elion, L. J. Geerligs, and J. E. Mooij. Field-induced superconductor-to-insulator transitions in josephson-junction arrays. *Phys. Rev. Lett.*, 69:2971–2974, Nov 1992.

[44] A. J. Rimberg, T. R. Ho, Ç. Kurdak, John Clarke, K. L. Campman, and A. C. Gossard. Dissipation-driven superconductor-insulator transition in a two-dimensional josephson-junction array. *Phys. Rev. Lett.*, 78:2632–2635, Mar 1997.

[45] C. G. L. Bøttcher, F. Nichele, J. Shabani, C. J. Palmstrøm, and C. M. Marcus. The Berezinskii-Kosterlitz-Thouless Transition and Anomalous Metallic Phase in a Hybrid Josephson Junction Array, October 2022. arXiv:2210.00318 [cond-mat].

[46] TexasPowerfulSmart. Electron beam resists, 2022.

[47] Jorden Senior. Lecture notes on dilution refrigerators, May 2021.

[48] Jack Ekin and George Zimmerman. Experimental techniques for low-temperature measurements: Cryostat design, material properties, and superconductor critical-current testing. *Physics Today - PHYS TODAY*, 60, 05 2007.

[49] David M Pozar. *Microwave engineering; 3rd ed.* Wiley, Hoboken, NJ, 2005.

[50] A. A. Clerk, M. H. Devoret, S. M. Girvin, F. Marquardt, and R. J. Schoelkopf. Introduction to Quantum Noise, Measurement and Amplification. *Reviews of Modern Physics*, 82(2):1155–1208, April 2010. arXiv:0810.4729 [cond-mat, physics:quant-ph].

A. Calculation of Thermal Noise

The net thermal noise seen by each microwave measurement line in the fridge can been calculated based on total attenuation along the line. The following analysis and calculations are based on work done by PhD student Soham Mukhopadhyay. The attenuators are needed to ensure that the incoming signal seen at the sample and cryogenic circuit elements is not so high as to cause damage. An attenuator can be modeled as a beam splitter, that takes an incoming signal and passes both the signal and some amount of thermal noise due to the attenuator. If the incoming signal is S, the attenuation in dB is n, and the added thermal noise is T, then the combined output of the 'splitter' is $nS + (1-n)T$. On lines 1-3 and 6-7 there is 50 dB of attenuation, on line 4 there is only 20 dB of attenuation. Lines 5 and 8 have no attenuation as they are output lines, and have amplifiers installed. The attenuation of n dB's is $10^{-n/10}$. To calculate the noise at each stage one must take into account the temperature of the previous stage, multiply by the attenuation, and then add the noise due to the temperature of the current stage. The calculation of thermal noise seen at each stage of the fridge for lines 1-3 and 6-7 is as follows:

$$70\,\text{K stage, } 0\,\text{dB: } 300 \cdot 10^{0} + (1 - 10^{0}) \cdot 70 = 300\,\text{K} \tag{A.1}$$

$$4\,\text{K stage, } 20\,\text{dB: } 300 \cdot 10^{-2} + (1 - 10^{-2}) \cdot 4 = 6.96\,\text{K} \tag{A.2}$$

$$\text{Still stage (700 mK), } 10\,\text{dB: } 6.96 \cdot 10^{-1} + (1 - 10^{-1}) \cdot 0.7 = 1.33\,\text{K} \tag{A.3}$$

$$\text{Cold stage (100 mK), } 0\,\text{dB: } 1.33 \cdot 10^{0} + (1 - 10^{0}) \cdot 0.1 = 1.33\,\text{K} \tag{A.4}$$

$$\text{Mixing chamber (10 mK), } 20\,\text{dB: } 1.33 \cdot 10^{-2} + (1 - 10^{-2}) \cdot 0.01 + \hbar\omega/2 = 23.2\,\text{mK} \tag{A.5}$$

The $\hbar\omega/2$ term in the last line comes from zero point fluctuations due to the vacuum. This only becomes relevant at such low temperatures, which is why it is not included in earlier stages. A very similar calculation can be carried out for line 4 with only 20 dB total attenuation. The thermal noise on lines 5 and 8 is not relevant, as these are output lines and do not affect the temperature seen at the sample. A temperature of about 23 mK is typically observed in the fridge setup, indicating that these calculations are correct.

B. Calculation of Thermal Conductance

The choice whether to grease an interface before installing a component in the fridge is more complicated than it seems at the outset. To illustrate the difference grease can make in increasing the thermal conductivity of two components, a short calculation is presented below. Assuming a small gold-plated amplifier is bolted to a gold-plated bracket with a small M1.6 screw, what is the thermal conductance across the 2x2 cm surface area?

Using values from table A3.4 and figure 2.7 of [48], the force generated by an M1.6 screw in gold with a factor of two safety margin is nearly 222 N/50 lb (approximated from the load limit of aluminum). If the amplifier is installed on the 4 K plate, the heat flow between the two components is calculated as follows:

$$\dot{q}/\Delta T = (5 \cdot 10^{-1}\,\mathrm{W/K})(50\,\mathrm{lb}/100\,\mathrm{lb}) \tag{B.1}$$

$$= 2.5 \cdot 10^{-1}\,\mathrm{W/K} \tag{B.2}$$

But if grease is applied in between the surfaces:

$$\dot{q}/\Delta T = (10^{-1}\,\mathrm{W/K})((2\,\mathrm{cm})^2/(1\,\mathrm{cm})^2) \tag{B.3}$$

$$= 4 \cdot 10^{-1}\,\mathrm{W/K} \tag{B.4}$$

There is 1.6 times better heat conductance when grease is applied between the gold interfaces. This difference becomes even more dramatic when materials such as copper are used instead of gold, as in the example shown in section 2.7 of [48], or at comparatively higher temperatures such as 70 K.

C. Dissipated Power Calculations

In the course of designing the physical experiment, it became important to calculate the realistic parameters for various circuit elements. It was important that our experiment could be carried out in a regime where the power delivered to the load resistor would be at a maximum - so that the noise power could have the best chance at being resolved. To do this, we calculated the power vs frequency plots for various system parameters. We used the parameters of the sample that we ended up fabricating, and the equation given in section 3 of this thesis. The results are shown below in C.1. The capacitance is calculated using the sample area, the distance separating the gate from the sample, the dielectric constant for the materials used, and the vacuum dielectric constant:

$$C = \epsilon_0 \cdot \epsilon_r * A/d \tag{C.1}$$

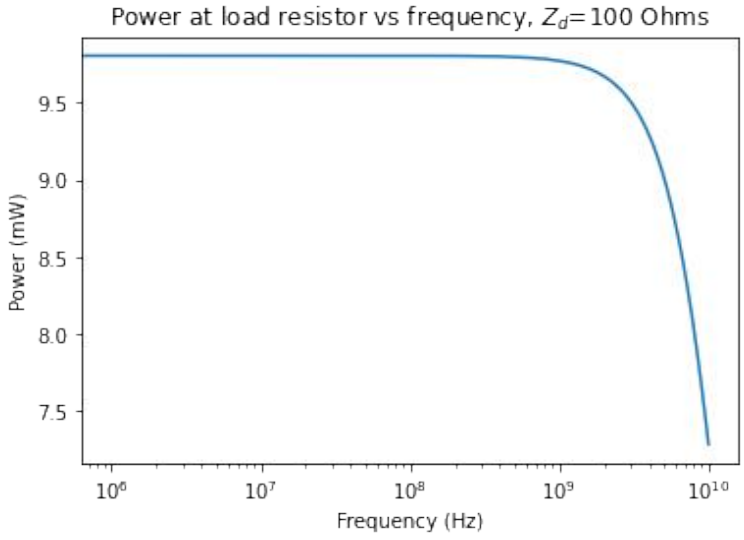

Figure C.1.: Device resistance 100 Ω, device capacitance of 9.44 pF. The corner frequency of this device is a little over 5 GHz. An input voltage of 2 V was assumed.

A corner frequency of 5 GHz doesn't allow much room for experimentation, as it may end up that doing measurements in a higher frequency band, such as 4-8 GHz may be prudent. So we may have to adjust the parameters so that the capacitance is larger. See the next plots C.2 and C.3.

By decreasing the capacitance slightly, as a result of increasing the separation distance of the gate to the sample from 15 nm to 40 nm, and decreasing the size of the sample slightly, we achieve corner frequencies above the range that we are interested in (11 GHz for a device

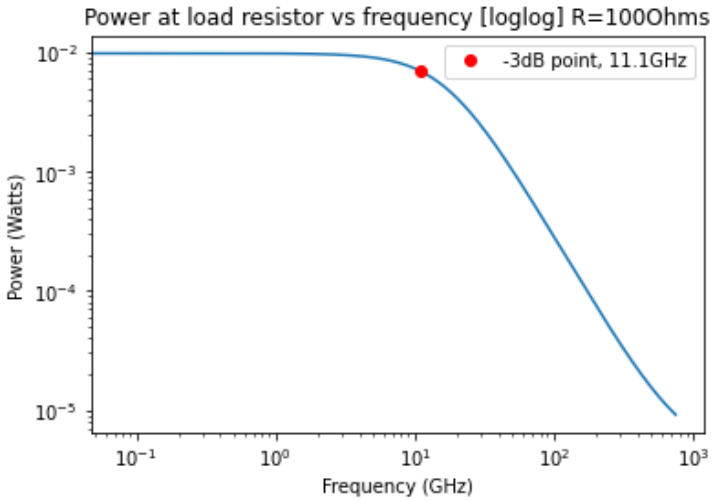

Figure C.2.: Device resistance 100 Ω, device capacitance of 9.37 pF. The 3 dB point is shown on the plot to be 11.1 GHz.

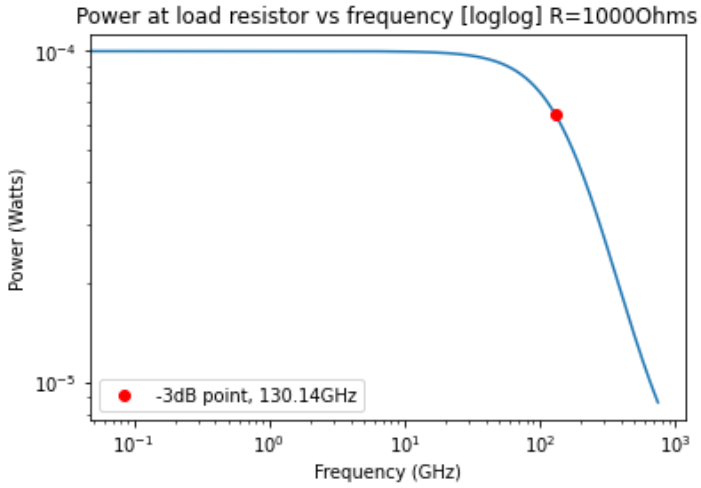

Figure C.3.: Device resistance 1 kΩ, device capacitance of 9.37 pF. The 3 dB point is shown on the plot to be 130.14 GHz.

resistance of 100 Ω and 130 GHz for a device resistance of 1 kΩ. The 3 dB point is the frequency at which the power has decreased by 3 dB from its maximum value, signifying a significant drop in power, after which it will no longer be prudent to measure.

These calculations settled our decision to fabricate a device with these parameters, and assured us that it would be possible to measure the device in the frequency ranges available to us. The ability to resolve the noise power at frequencies between 1 and 8 GHz was of utmost importance, and these calculations show that it should, in principle, be possible.

D. Supplemental figures for PCB Development

Many additional data were taken while experimenting with and figuring out the new PCBs, too many to be included in this thesis. In this appendix are gathered some of the figures that may help illustrate the points made in chapter three of this thesis.

The first figure, figure D.1, compares the second and third iteration of the PCB, in which the third iteration has had the inductors removed. This illustrates that the inductors were the source of new resonances in the spectrum, and that without them the PCB behaves similarly to the second iteration.

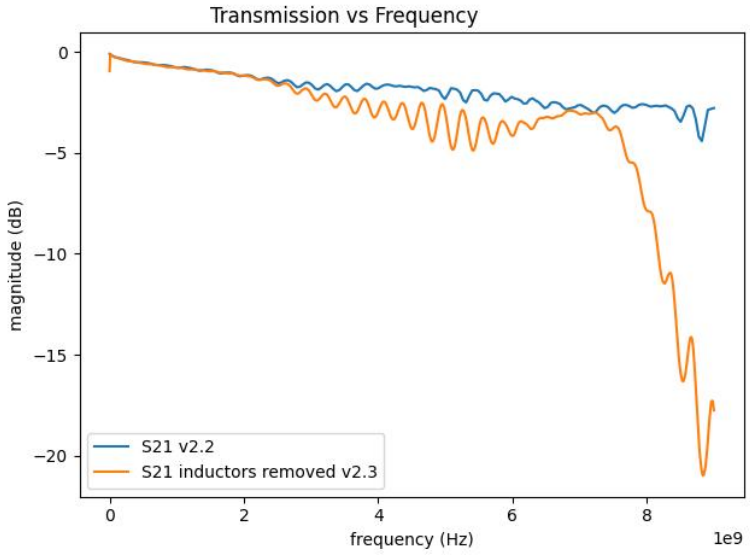

Figure D.1.: Comparison of the PCB version two with the PCB version three without inductors.

We also experimented with different capacitor values, hoping to see how the resonances/spectrum shifted around with shifting capacitance. We observed that higher capacitances shifted the spectrum higher in frequency, revealing a corner frequency near zero, and higher capacitances also suppressed some of the resonances. Shown in figure D.2.

The first thing weI checked with the fourth iteration of the PCB was the S21 magnitude vs frequency trace for just the microwave line with bias tees. The result was a fairly smooth transmission between 2-7 GHz, with a lot of roll-off at low frequency and some un-interesting

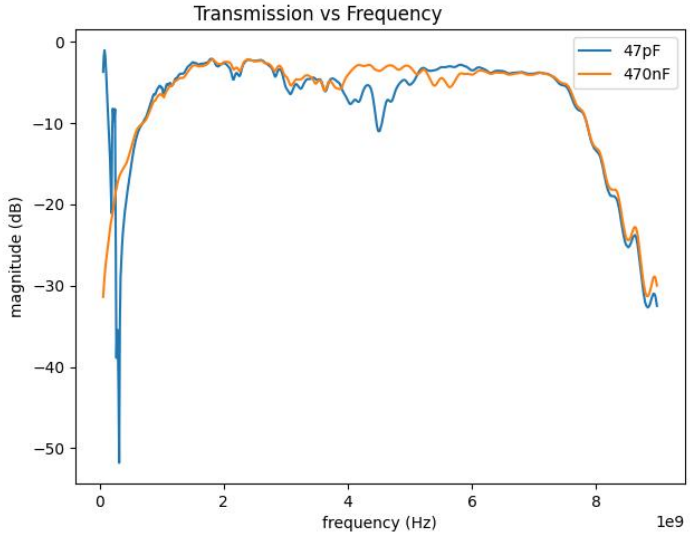

Figure D.2.: Comparison of S21 data from 47pF capacitors with S21 data from 470nF capacitors on PCB version three.

dips above 8 GHz. Shown in figure D.3.

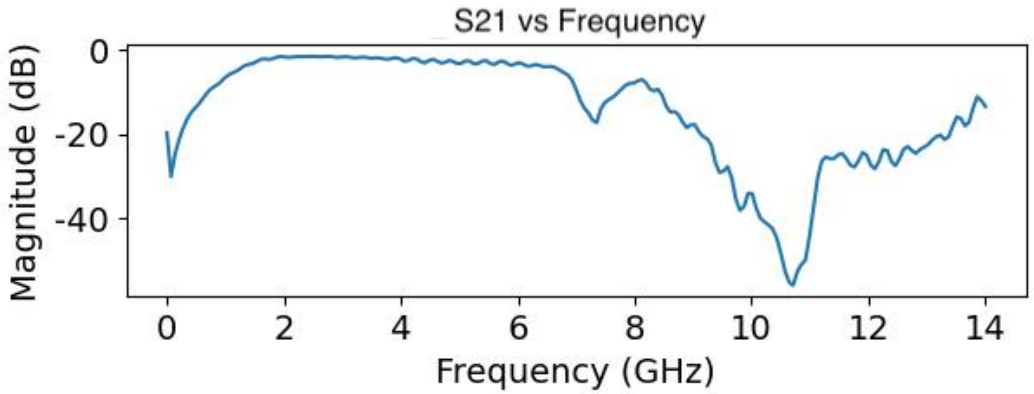

Figure D.3.: S21 magnitude vs frequency for PCB v4.

To be sure that the roll-off wasn't being caused by the capacitors alone we removed the inductors from the PCB. This resulted in a trace that looked very similar to PCB version two and version three without inductors which was again encouraging, that the underlying nature of the PCB hadn't changed despite the alterations we had made. Shown in figure D.4.

Now presented is the data for other inductors used on the PCB that were ultimately decided against. The 33 nH inductor series is presented in figure D.5. The 82 nH inductor series is presented in figure D.6. The 10 nH inductor series is presented in figure D.7. From these figures it is clear that the 82 nH and 10 nH inductors resulted in more resonances and fewer/smaller smooth bands. Because of this, the choice of inductance came down to the 33 nH or 15 nH inductors. Ultimately we went with the 15 nH inductors because there

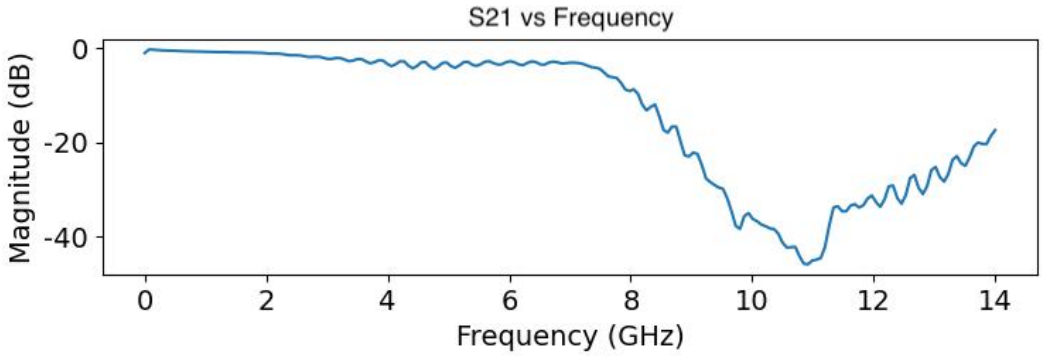

Figure D.4.: S21 vs frequency for PCB v4 without inductors.

was slightly less insertion loss at high frequencies than with the 33 nH inductors, while also maintaining low insertion loss at low frequencies, making the 15 nH inductors the most flexible option.

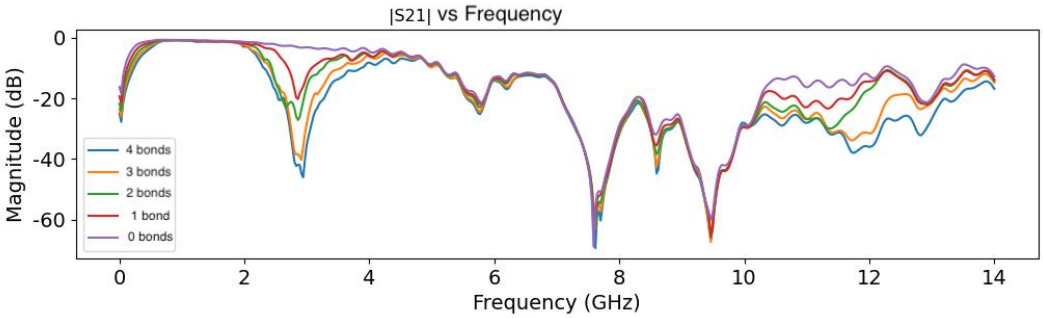

Figure D.5.: 33 nH inductors, plucking wire bonds off one by one.

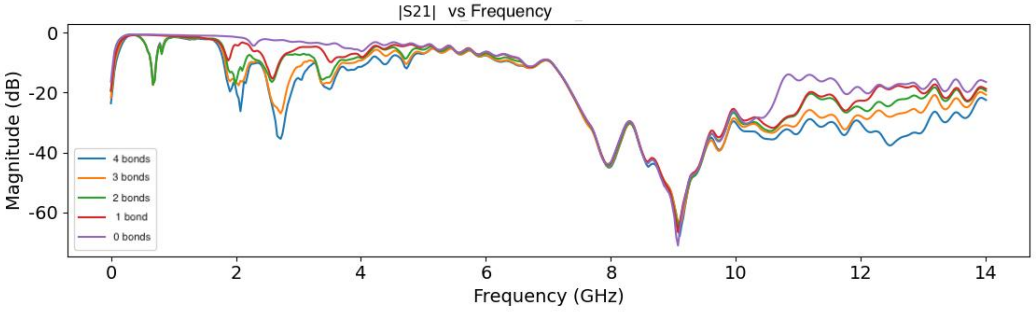

Figure D.6.: 82 nH inductors, plucking wire bonds off one by one.

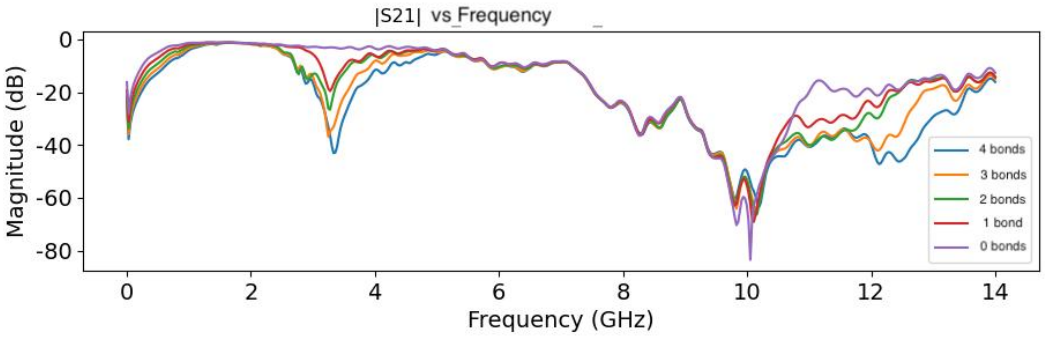

Figure D.7.: 10 nH inductors, plucking wire bonds off one by one.

E. Supplemental Figures for Coaxial Cable Installation

The supplemental S21 magnitude vs frequency and S21 phase vs frequency figures of the superconducting coaxial cables installation is presented here. First the installation between mixing chamber and cold plate in figure E.1, and then between the cold plate and the still plate in figure E.2, and finally between the still plate and the input of the amplifier on the 4 K plate in figure E.3. It can be seen from the data that there are no unexpected resonances which indicates that the coaxial cables are not damaged, and the insertion loss for each coaxial cable around 1 GHz is less than 3 dB.

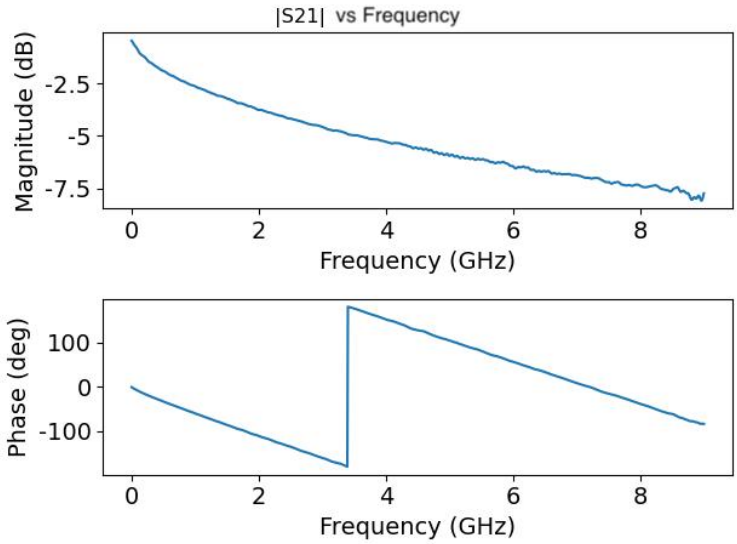

Figure E.1.: Superconducting coaxial cable installation check between mixing chamber and cold plate.

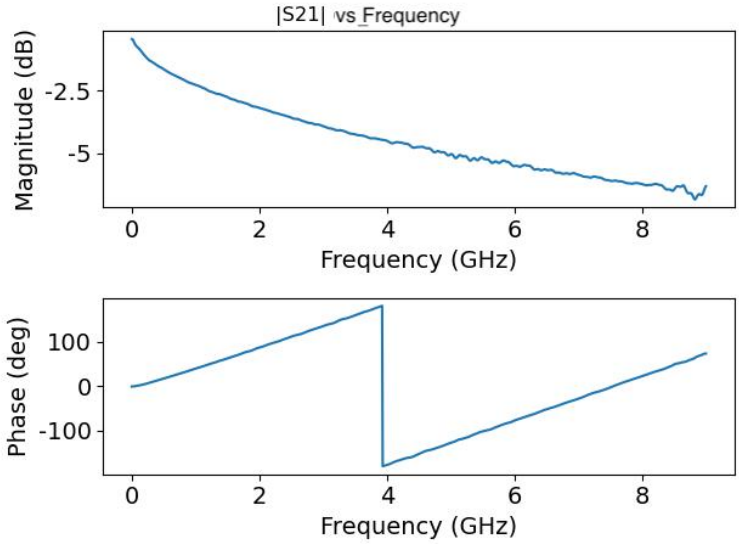

Figure E.2.: Superconducting coaxial cable installation check between cold plate and still plate.

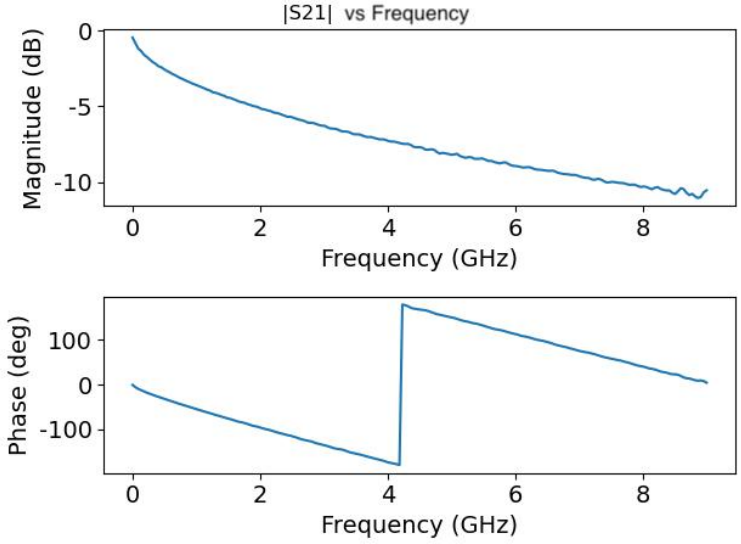

Figure E.3.: Superconducting coaxial cable installation check between still plate and the input port of the amplifier on the 4 K plate.

F. Simulations of On-chip Microwave Coupler

Using Sonnet simulation software, we performed several simulations of various configurations of on-chip microwave couplers. The idea was to find a configuration that maximized coupling to the co-planar waveguide on the device from the microwave transmission line. The performance of a co-planar waveguide depends on the dielectric constant of the material beneath the conductors, the thickness of this material, the spacing between the ground planes and the center conductor, and the thickness of the center conductor. The first simulation (see figure F.1) showed a coupling from the microwave coupler to the sample of about 0.4 % at 6 GHz. In the second iteration we changed the shape of the simulation space to be square and the coupling increased to 1 % at 6 GHz (see figure F.2).The third iteration increased the length of the coupler and brought it closer to the central conductor (see figure F.3, and achieved a coupling of 1.6 % at 6 GHz. The final iteration that became the plan for the chip design is shown in figure F.4, where a coupling of about 4 % at 6 GHz was reached.

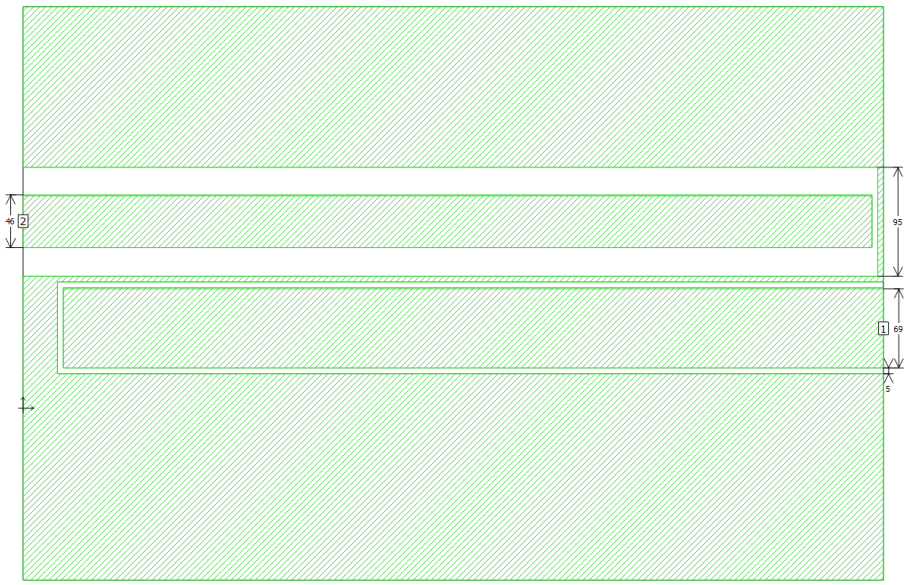

Figure F.1.: Starting point of the simulations. Dimensions were estimated from standard co-planar waveguide equations.

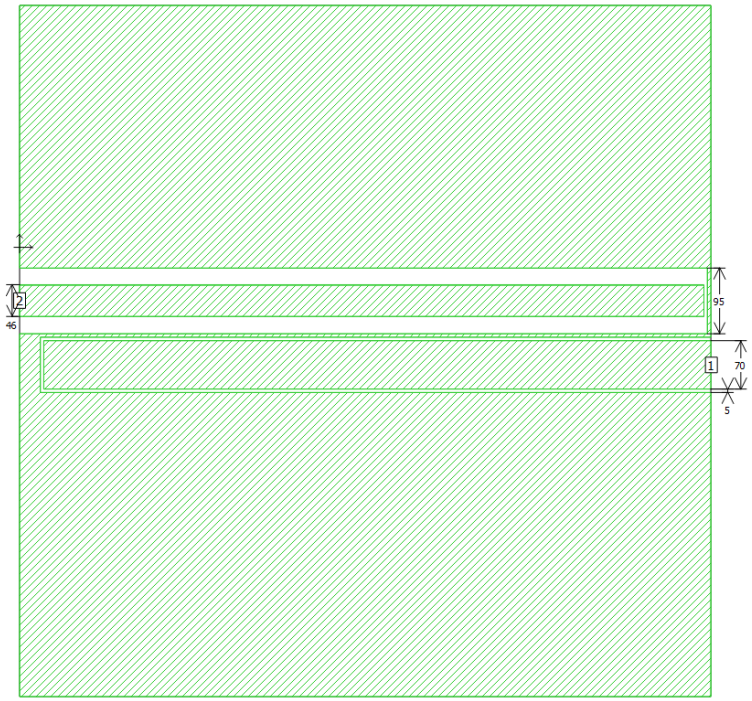

Figure F.2.: Iteration two of the simulations.

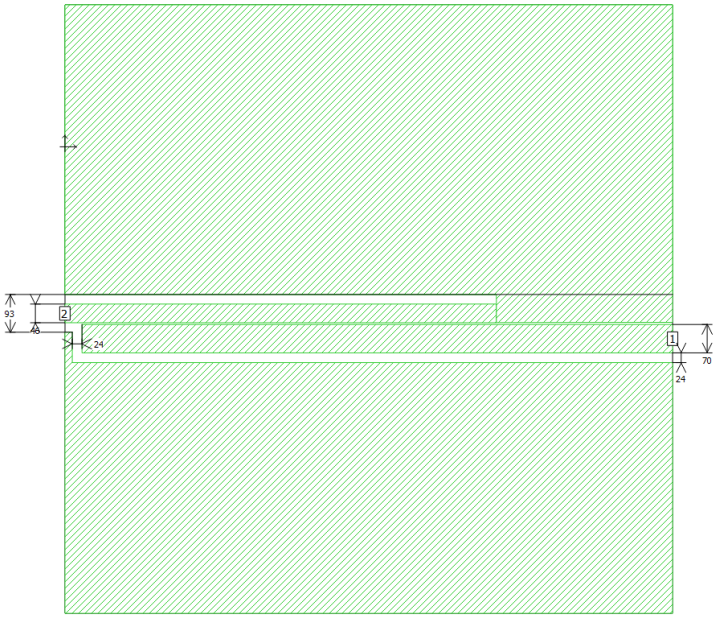

Figure F.3.: Iteration three of the simulations.

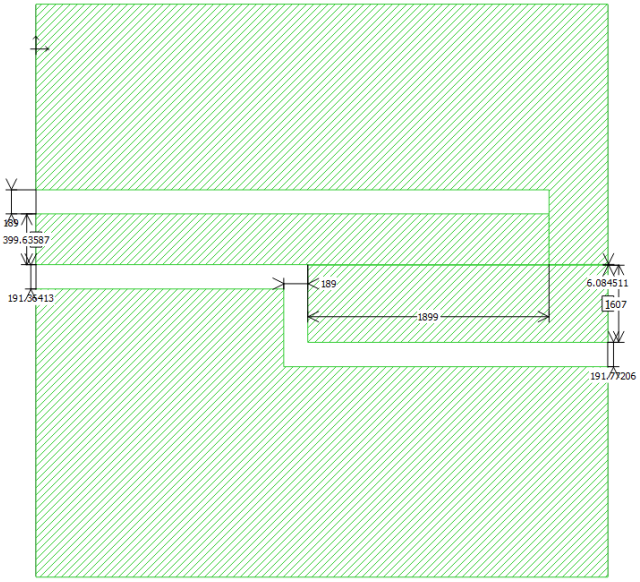

Figure F.4.: The final iteration of the simulations.

G. Room Temperature Measurement Setup

In this section is an overview of the room temperature measurement schemes, both in microwave and transport measurements. Both measurement setups interface with a data acquisition computer (not pictured), where every instrument can be controlled remotely via the computer. The microwave setup is shown in figure G.1. There the fridge can be seen on the right, and the bunch of blue microwave cables that bring the signal into and out of the fridge are slightly hidden behind the cart. The power supply for the amplifier is on top of the cart, and the BNC cable on the front of it goes to the top of the fridge, where it connects to the fischer cable that then brings the power to the amplifier inside the fridge. The Keithley voltage supply on the top left is not part of the microwave measurement chain, but rather it provides the voltage that goes to the gate of the device via the breakout box in the DC measurement setup. The VNA is dark gray and located near the bottom of the photo, behind the plexiglass and underneath a blue RF switch. The VNA can be connected to the microwave cables. Not pictured is the spectrum analyzer used in the experiment for measuring noise, it usually sits to the left of the VNA. The measurement chain is changed between the output being the VNA or the spectrum analyzer as well as whether the input is coming from a reflection or transmission measurement via the RF switch on top of the VNA.

The transport setup is shown in figure G.2. On the far left is the computer that controls the fridge as it cools down or warms up. Then there is the digital multimeter (DMM) that reads the output current or voltage. Underneath the DMM is the lock-in amplifier which is used to measure the resistance of the device. On the right is the breakout box. This is the interface between the DC lines on the device and the rest of the measurement instruments. Each DC line has a terminal on the box, denoted by a number and a switch. As seen in the photo, there are cables plugged into some of the terminals. Those cables can then be plugged into the current source or the voltage source shown below. The breakout box has an output as well just to the right of the voltage source, that goes to the DMM.

,

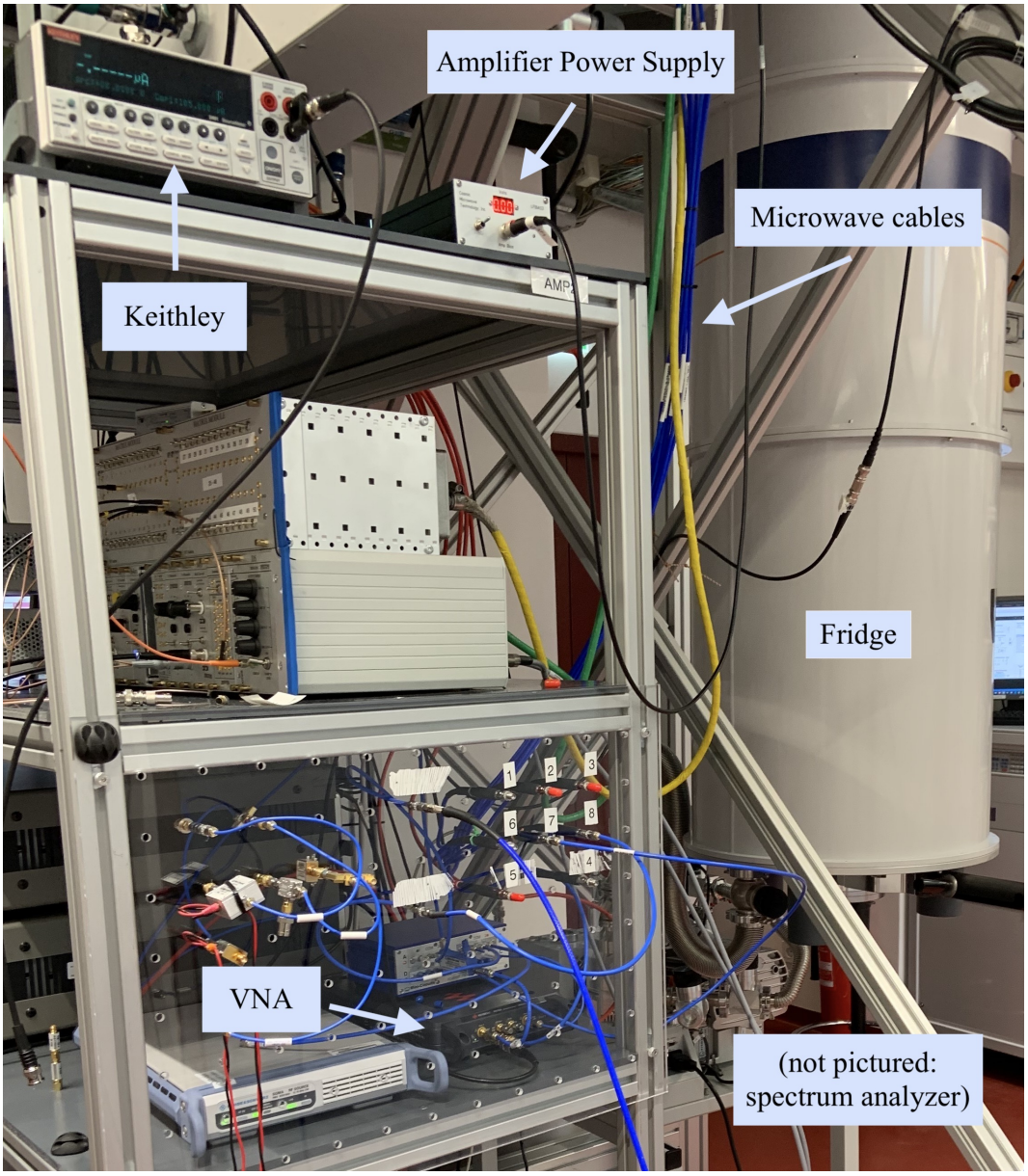

Figure G.1.: Photo with captions naming each of the instruments used in microwave measurements.

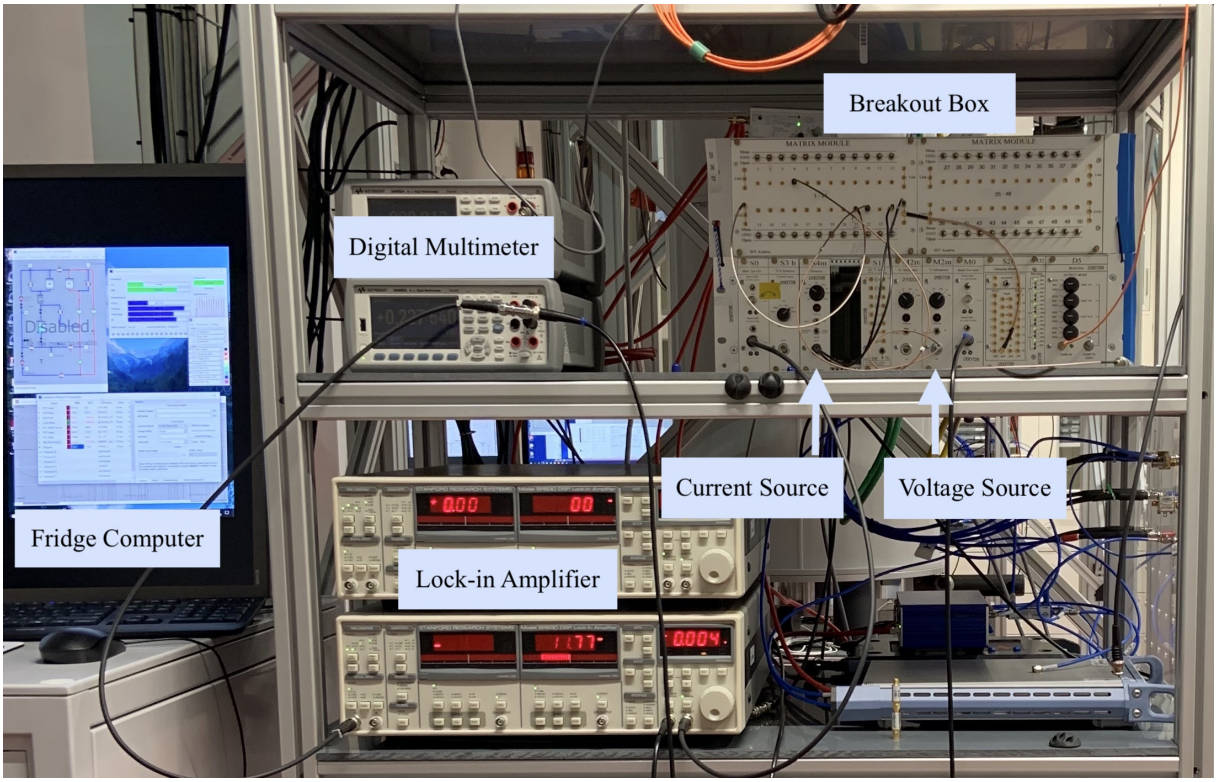

Figure G.2.: Photo with captions naming each of the instruments used in transport measurements.